

# The implications of Mexican-hat mirrors: calculations of thermoelastic noise and interferometer sensitivity to perturbation for the Mexican-hat-mirror proposal for advanced LIGO

R. O’Shaughnessy\*

*Theoretical Astrophysics, California Institute of Technology, Pasadena, CA 91125*

S. Strigin and S. Vyatchanin

*Physics Faculty, Moscow State University, Moscow, Russia*

(Dated: Received ?? Month 2003, printed November 13, 2018)

Thermoelastic noise will be the most significant noise source in advanced-LIGO interferometers with sapphire test masses. The standard plan for advanced-LIGO has optimized the optics, within the framework of conventional mirrors, to reduce thermoelastic noise. Recently, we and our collaborators have proposed going beyond the bounds of traditional optics to increase the effective beam spot size and thus lower thermoelastic noise. One particular proposal for mirror shapes (“Mexican-hat mirrors”) yields the class of “mesa” beams.

In this paper, we outline a general procedure for analyzing light propagating in individual arm cavities, and the associated thermoelastic noise, in the presence of arbitrary optics. We apply these procedures to study the Mexican-hat proposal. Results obtained by the techniques of this paper were presented elsewhere, to demonstrate that the Mexican-hat proposal for advanced-LIGO both significantly lowers thermoelastic noise and does not significantly complicate the function of the interferometer.

PACS numbers: 04.80.Cc, 07.60.Ly, 42.55.-f

## I. INTRODUCTION

Thermoelastic noise will be the dominant noise source in the advanced LIGO interferometers for frequencies at which they are most sensitive, should the advanced LIGO upgrade follow the baseline design [1, 2]. Other noise processes (e.g., conventional bulk thermal noise; coating thermal noise; unified optical noise) could be important, but are expected to be smaller in noise power, by a factor  $\sim 9$  (at the minimum of the noise curve), than thermoelastic noise. As a result, the sensitivity of the advanced LIGO interferometers can be significantly increased.

In a companion paper—the mesa-beam interferometer paper (MBI) [4], summarized briefly in a short LIGO technical document (MBI-S) [5]—we and our collaborators have argued that a significant reduction in thermoelastic noise can be achieved by using modified optics that reshape the beam from a conventional (gaussian) profile into a *mesa-beam* shape. We furthermore performed calculations which imply (though do not comprehensively demonstrate) that this proposal would not place significant burdens on the experimental community (e.g., in the need for slightly improved tilt control systems and improved mirror figure accuracies).

The companion publications (MBI and MBI-S) survey the physically and practically relevant features of our proposal—that is, they demonstrate that the proposal should work, and sketch how to implement it. Those publications intentionally omitted many supporting de-

tails, to be provided in this paper and a companion paper by Erika D’Ambrosio [6]. In particular, this paper provides the computational details underlying our evaluations of thermoelastic noise in various interferometer configurations; both this paper and D’Ambrosio [6] provide computational details of our studies of the influence of mirror imperfections (tilts, displacements, figure errors) on interferometer performance.

Further, this paper considers a broader class of possible improvements than MBI. The MBI paper discussed using mesa beams reflecting off of the standard advanced LIGO cylindrical mirrors. In this paper, we analyze mesa beams reflecting off more generically shaped mirrors—not merely cylinders of different dimensions, but also frustum-shaped mirrors.<sup>1</sup>

### A. Outline of paper

In this paper, we provide details behind the calculations discussed in MBI. For the reader not familiar with the principles behind thermoelastic noise, cavity optics, and cavity perturbation theory, the next four sections (Sections II, III, IV, and V) provide a brief review of the equations and computational techniques we employ. To be more explicit, in Sec. II we describe how to construct an idealized interferometer based on mesa beams while

---

<sup>1</sup> A frustum is a geometric shape arising between two parallel planes that intersect an axisymmetric cone perpendicular to the cone’s axis.

---

\*Electronic address: oshaughn@caltech.edu

remaining within LIGO design constraints (i.e. losses per bounce). [In the process, we also briefly review the theory of and introduce notation for optical cavity eigenfunctions and propagation operators.] We assume this interferometer, which has mesa beams resonating within the arm cavities, is driven by conventional (i.e. Gaussian) lasers, as described in Sec. III. In Sec. IV, we discuss how to analyze, via perturbation theory, the influence of mirror errors on interferometer performance. [In Section VII we will apply this general formalism to mirror transverse position errors (displacement), orientation errors (tilt), and figure error (shapes).] Finally, in Sec. V, we describe how we numerically implemented the calculations described in Sections II and IV. With those tools established, in Sections VI and VII we closely follow the arguments of MBI, carefully explaining the details behind those arguments.

Specifically, in Sec. VI, we use explicit forms for the mesa beam and its diffraction losses presented in Sections II and V to determine which mesa beams can operate in a given cavity, when the mesa beams are reflecting off of the standard advanced LIGO mirrors (i.e. cylinders of radius 15.7 cm and thickness 13 cm), as well as off mirrors of more generic shape (i.e. other cylinders and frustums). We then employ an expression for the thermoelastic noise associated with a given mirror and beam configuration (developed generally in Sec. II and discussed practically in Sec. V) to determine the thermoelastic noise associated with a given configuration. Table IV summarizes our results for designs which produce lower thermoelastic noise than the baseline advanced LIGO design.

Section VII describes how sensitive an interferometer using Mexican-hat mirrors will be to perturbation. More explicitly, Sections VII A, VII B, and VII C demonstrate by way of explicit comparison that arm cavities using spherical and mesa-beam mirrors appropriate to advanced LIGO are roughly equally sensitive to perturbations. Section VII C describes how sensitive the overall interferometer (as measured by its cavity gain, its dark port power, and its thermoelastic noise) will be to tilt perturbations. Finally, Section VII E determines how sensitive (as measured by cavity gain, dark port power, and thermoelastic noise) a mesa-beam advanced LIGO design without signal recycling would be to mirror figure errors.

Augmented by additional results discussed in MBI, which demonstrate that the full interferometer including signal recycling will be only moderately more sensitive, we conclude mesa-beam interferometers could be used in advanced LIGO without serious concern.

#### *Guide to reader*

The MBI paper reports the *results* of calculations developed in this paper and in one by Erika D’Ambrosio [6], emphasizing their practical significance. On the other hand, this paper emphasizes the *method* by which those

results were obtained. As a result, this paper has a dramatically different structure than MBI: two of the first sections (Sections II and IV) outline the equations that we have solved; the next section, Section V, describes how we solved them; and two of the last sections, Sections VI and VII, briefly summarize the specific technical results quoted in MBI and explain how those results were obtained.

The reader who wants only a cursory survey of the techniques used to obtain the MBI results should skim Sections II-IV, emphasizing the summaries in Sections II E and IV E; this reader should completely skip over the implementation section (Sec. V). Indeed, we recommend that a reader interested primarily in better understanding results presented in MBI should work *backwards*, first establishing a *cross-reference* between a result in MBI and a result in Sec. VI or VII of this paper, then reading in this paper the material surrounding the cross-reference.

On the other hand, a reader who wishes to verify or generalize our computations should read this paper from beginning to end.

#### **B. Connection with other published work**

The MBI paper [4] and the MBI-S LIGO technical document [5] survey our results, emphasizing their practical significance to advanced LIGO interferometer design. This paper provides details behind many relatively lengthly analytic or numerical calculations which those papers touched upon only briefly.

Another of our MBI collaborators, Erika D’Ambrosio, has performed many of the same calculations (e.g., the sensitivity of the interferometer to tilt and to defects) using a sophisticated, standard, and trusted tool—the so-called “FFT code”—designed and developed specifically to study the behavior of general interferometers [6]. As noted in MBI and in her paper, our two independent approaches agree well.

#### **C. Notation**

##### *1. Symbols*

*b* The natural diffraction length scale (i.e. Fresnel length) associated with the previous two parameters:  $b \equiv \sqrt{L/k} = 2.6$  cm.

$C_V$  Specific heat of test mass, per unit mass, at constant volume

*D* Mesa beam characteristic scale, Eq. (5).

*E* Young’s modulus. An elastic parameter in the stress tensor for an isotropic material [Eq. (10b)]. (See Appendix A for a discussion of the explicit value used.)

- ETM End test mass of an arm cavity (i.e. the mass opposite the end light enters the cavity).
- $F_o$  The net force applied to the front face of the the mirror in the thermoelastic model problem of Sec. IIB; cf. Eqs. (8) and (9).
- $f$  Frequency, units  $s^{-1}$ . Typically, we are interested in values of  $f$  near the peak sensitivity of LIGO (i.e.  $f \approx 100\text{Hz}$ ).
- $g_{ab}$  Metric of 3-space. (See comments on tensor notation, below).
- $h_{1,2}$  Height of mirror 1's (or 2's, respectively) surface.
- $I$  Thermoelastic noise integral, Eqs. (8) and (9).
- ITM Input test mass of an arm cavity.
- $k$  The wavevector of light in the cavity,  $k = 2\pi/\lambda$  with  $\lambda = 1064\text{nm}$ .
- $k_b$  Boltzmann's constant [ $1.38 \times 10^{-16}\text{g cm}^2 \text{s}^{-2}\text{K}^{-1}$ ]
- $L$  The length of the LIGO arm cavity [ $L = 3.99901\text{km}$ ].
- $\mathcal{L}$  Some number associated with diffraction losses. When used alone, denotes the total diffraction losses associated with one round trip through the cavity. When given certain subscripts, as with  $\mathcal{L}_1$ , denotes the clipping-approximation estimate of diffraction losses associated with a single reflection off of mirror 1.
- $M$  Mass of the test mass [40 kg].
- MBI The mesa-beam interferometer paper [4].
- $P(r)$  The intensity distribution of laser light in a cavity, normalized to unity (i.e.  $\int P(r)d(\text{area}) = 1$ ).
- $\vec{r}$  A vector transverse to the optic axis of the cavity (i.e. two-dimensional).
- $s$  Transverse displacement of an arm cavity's ETM.
- $T_{ab}$  Elastic stress tensor for an isotropic medium, Eq. (10b). (See comments on tensor notation, below).
- $u$  Electric field on some plane in the arm cavity (typically, the face of the ITM, propagating away from the ITM), renormalized to unit norm (i.e.  $\int |u|^2 d(\text{area}) = 1$ ). Subscripts identify the specific system  $u$  refers to.
- $y^a$  The displacement vector field associated with an elastic distortion.
- $x, y$  The cartesian components of the 2-vector  $\vec{r}$ .
- $z$  A coordinate measured along the optic axis of the cavity (i.e. in a direction perpendicular to  $\vec{r}$ ).
- $\hat{z}^a$   $\hat{z}$  is a unit vector pointing in the positive  $z$  direction;  $\hat{z}_a = \hat{z}^a$  are the components of this vector in our coordinates. For example, in cartesian coordinates  $\hat{z}_a = 1$  if  $a = z$  and 0 if  $a = x, y$ .
- $\alpha_l$  Coefficient of linear thermal expansion, assumed isotropic. For an isotropic material, the differential change in volume with temperature is  $dV/dT/V = 3\alpha_l$ . (See Appendix A.)
- $\alpha_{1,2}$  Norm of the first- and second-order corrections to the optical state of the cavity when the mirror is tilted [i.e. in Eqs. (62) and (63)].
- $\kappa$  Thermal conductivity, assumed isotropic (see Appendix A).
- $\eta$  An eigenvalue of Eq. (13).
- $\lambda$  An eigenvalue of Eq. (28).
- $\rho$  Density of test mass. (See Appendix A.)
- $\sigma$  Poisson ratio. An elastic parameter in the stress tensor for an isotropic material [Eq. (10b)]
- $\theta$  An angle through which the mirror is tilted.
- $\Theta$  The expansion associated with a displacement field  $\Theta = \nabla_a y^a$  [e.g., in Eq. (9)]. Also denotes a unit step function [e.g., Eq. (11c)].
- $\omega = 2\pi f$ .
- $\zeta_{1,2}$  Norm of the first- and second-order corrections to the optical state of the cavity when the mirror is displaced [i.e. in Eqs. (57) and (58)].
- $\zeta_m$  Used *only* in Eq. (43),  $\zeta_m$  denotes the  $m$ th zero of  $J_1(x)$ .

## 2. Tensor notation

The elasticity calculations (e.g., involving the elasticity tensor  $T_{ab}$ ) involve tensors. While the authors prefer to interpret these expressions with an abstract tensor notation (i.e. Wald [7]), the reader may without loss of generality use global cartesian coordinates and interpret the latin indices  $a$  and  $b$  as running from  $1 \dots 3$ , indexing the coordinate directions; in these coordinates, upper and lower indices are entirely equivalent (e.g.  $y^a = y_a$ ). In this case, the reader should interpret  $\nabla_a$  as the coordinate partial derivative  $\partial/\partial x^a$  and  $g_{ab}$  as the  $3 \times 3$  identity matrix.

## 3. State and operator notation

As explained briefly in Sec. IIC1, because propagation of the state of the field from one plane to another

is merely a unitary transformation, we substantially simplify the many integral-equation operations by using a quantum-mechanics-style notation for the operators. For example, the integral operation

$$E(\vec{r}', z') = \int d^2r U(\vec{r}', z'; \vec{r}, z)E(\vec{r}, z) \quad (1)$$

is represented as

$$E(z') = U(z', z)E(z). \quad (2)$$

Further, typically the relevant planes (i.e. the  $z, z'$ ) are known, and omitted, in expressions like the above.

Under a similar philosophy, we also use quantum-mechanics-style notation for the values of the electric field on a specific plane; in other words, we represent states of the optical cavity using quantum-mechanical state notation. For example, the optical state of the cavity may be equivalently denoted by the explicit functional form  $u$  or  $u(\vec{r})$ , or alternatively as the state vector  $|u\rangle$ . In a similar spirit, we index the potential solutions to the eigenequation [Eq. (28)] by an integer  $p$ , and denote the set of basis states as  $|p\rangle$ . More generally we can represent *any* function defined on a two-dimensional plane—not necessarily normalized; not necessarily a potential state—as a state vector.

We use this notation in particular to simplify notation for inner products between two states  $|u\rangle$  and  $|v\rangle$ :

$$\langle v|u\rangle \equiv \int d^2r v^*(r)u(r). \quad (3)$$

Finally, to simplify the frequent expressions that involve the norm of a state, we use the symbol  $\|\cdot\|$  to denote  $L^2$  norms:

$$\|u\|^2 \equiv \langle u|u\rangle = \int d^2r |u(\vec{r})|^2 \quad (4)$$

Many quantum mechanics textbooks written over the past half century employ this notation (cf., e.g., [8, 9, 10]).

## II. THEORY OF AN IDEALIZED MEXICAN-HAT ARM CAVITY

In this section, we review the equations needed to understand the design of an arm cavity which (i) uses mesa beams, (ii) reduces thermoelastic noise in an advanced LIGO interferometer, and (iii) satisfies advanced LIGO design constraints (i.e. the diffraction losses per bounce are less than the advanced LIGO design threshold of 10ppm, and the mirrors have mass 40 kg).

Specifically, we introduce the mesa beam, defined for the purposes of this paper by Eq. (5). We define the mirror surfaces which confine this beam by Eq. (6). From Eq. (5) we can determine the beam intensity profile. We can relate the beam intensity profile to the power spectrum of thermoelastic noise [Eq. (7)] via Eqs. (9) and

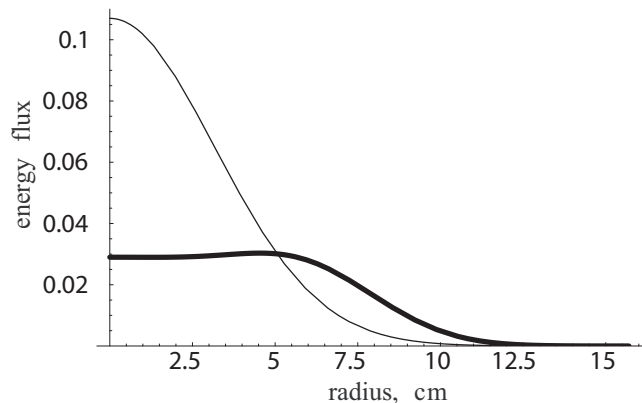


FIG. 1: The heavy solid curve is an example of a mesa beam’s intensity profile; the lighter curve is the intensity profile of a Gaussian beam with similar losses. More precisely, this curve shows the energy fluxes per unit area (normalized to unity) for the mesa beam (thick curve) and Gaussian beam (thin curve) that have 10ppm of diffraction losses on a mirror with coated radius 15.7 cm.

(10). Finally, we describe how to limit attention to only those mesa beams with low diffraction losses, using an approximate approach [the clipping approximation, Eq. (16)] which we will test against an exact expression [Eq. (15)].

### A. Mexican-hat mirrors and mesa beams

The mesa-beam interferometer (MBI) paper [4] presented explicit forms for certain specific mesa beams (“canonical mesa beams”) produced inside a cavity bounded by two *identical* mirrors. [In MBI, only the values of the beam fields at the surface of the ITM (specifically, values propagating away from the ITM surface) were given; Appendix B provides a more comprehensive discussion.] We summarize MBI Eqs. (2.3), (2.6), and (2.7) to provide a compact summary of how to compute the values  $u_{\text{mesa}}$  of a mesa beam’s normalized electric field on the mirror face, at radius  $r$  from the optic axis:

$$U(\vec{r}, D) = \int_{r' < D} d^2r' \exp \left[ -\frac{(\vec{r} - \vec{r}')^2 (1 + i)}{2b^2} \right] \quad (5a)$$

$$N^2(D) \equiv \int_0^\infty |U(D, r)|^2 2\pi r dr \quad (5b)$$

$$u_{\text{mesa}}(D, r) \equiv U(D, r)/N(D) \quad (5c)$$

where in the first integral the integration is over all points with  $r' \equiv |\vec{r}'| < D$ . [For readers who wish to numerically explore mesa fields themselves, note that MBI Eq. (2.5) provides a more efficient means of calculating the mesa amplitude function  $u(D, r)$ .] Figure 1 provides an example of a mesa-beam intensity distribution  $|u(D, r)|^2$ .

As discussed in Appendix B and in MBI Sec. II D [cf. MBI Eq. (2.13)], the mirrors that reflect mesa beams

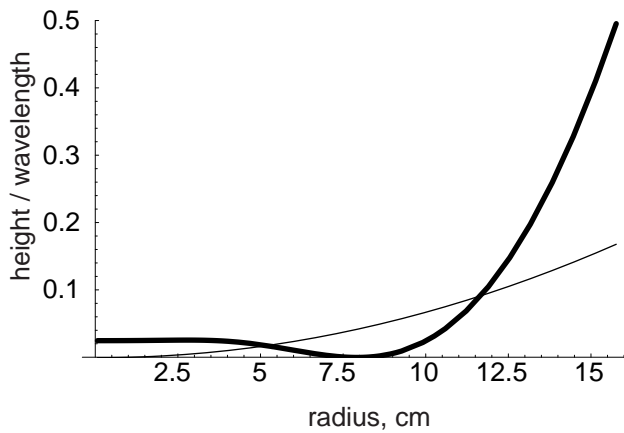


FIG. 2: The heavy solid curve is an example of a Mexican-hat mirror; the lighter curve is an example of a spherical (i.e. parabolic) mirror. More precisely, this curve shows the spherical and Mexican-hat mirrors which produce the beams described in Fig. 1

back into themselves (denoted *Mexican-hat mirrors*) necessarily have a continuous height function  $h_{\text{MH}}$  given by

$$kh_{\text{MH}} = \text{Arg}[u_{\text{mesa}}(D, r)]. \quad (6)$$

where  $k = 2\pi/\lambda$  is the wavenumber of light in the arm cavity. The solid curve in Figure 2 provides an example of a Mexican-hat mirror.

## B. Thermoelastic noise

Using the expressions in the previous section, one can design idealized interferometers which operate with mesa beams and Mexican-hat mirrors. The thermoelastic noise associated with the resulting interferometer design can be discovered with the techniques of Liu and Thorne (LT) [12], who employ Levin's direct method [13] to derive the following formula for an interferometers' thermoelastic noise in terms of a noise integral  $I_A$ :

$$S_h(f) = 4\kappa k_B \left( \frac{\alpha_l ET}{C_V(1-2\sigma)\rho\omega L} \right)^2 \sum_{A=1}^4 I_A; \quad (7)$$

cf. LT Eqs. (3), (4) and (13); the notation used here has been described in Sec. I C.

The sum on  $A = 1, 2, 3, 4$  is over the four test masses, and the quantity summed is the noise integral

$$I_A = \frac{2}{F_o^2} \int_{V_A} \langle (\vec{\nabla}\Theta)^2 \rangle d\text{volume}. \quad (8)$$

In Eq. (8),  $\Theta$  is the expansion (i.e. fractional volume change) resulting from a pressure—sinusoidally oscillating at frequency  $f = \omega/2\pi$ , proportional to the light beam intensity, with net force  $F_o$ —imposed on the face

of the mirror; the integral is over  $V_A$ , the volume of test mass  $A$ ; and the average  $\langle \dots \rangle$  is over one oscillation period  $1/f$ . [Note that the dimensions of  $I_A$  are length/force $^2 = \text{s}^4\text{g}^{-2}\text{cm}^{-1}$ .]

In the analysis that leads to the above expressions [Eqs. (7) and (9)], LT [12] have made certain idealizations and approximations, some better than others.<sup>2</sup> We shall employ this expression as it stands, using the precise parameter values provided in Appendix A.

### 1. Effective static elasticity model for $I_A$

For the frequencies at which advanced LIGO will be most sensitive ( $f \sim 100\text{Hz}$ ), the interior of the test mass will respond effectively instantaneously to the imposed pressure profile in the model problem described above.<sup>3</sup> As a result, by going to the accelerating frame of the test mass and following that accelerating frame for one period to simplify the average, we can approximate  $I_A$  by

$$I_A \approx \frac{1}{F_o^2} \int_{V_A} (\vec{\nabla}\Theta)^2 d\text{volume}. \quad (9)$$

where the expansion  $\Theta = \nabla_a y^a$  arises due to the response (i.e. local displacement field)  $y^a$  of the test-mass substrate to the following *static* conditions:

1. *Static (accelerating-frame) force*: Some net force  $F_o \hat{z}$  acts uniformly throughout the test mass (i.e. provides a force density  $F_o/V_A$ ). To be specific, using the equations for an isotropic elastic solid (cf. Blandford and Thorne [14]), the response field  $y^a$  satisfies

$$\nabla^a T_{ab} = \hat{z}_b F_o/V_A, \quad (10a)$$

$$T_{ab} \equiv -\frac{E}{(1+\sigma)(1-2\sigma)} \times \left[ \frac{(1-2\sigma)}{2} (\nabla_a y_b + \nabla_b y_a) + \sigma \Theta g_{ab} \right] \quad (10b)$$

<sup>2</sup> For example, they idealize the test-mass material as an isotropic material; however, the proposed test mass material, sapphire, is only moderately well approximated as isotropic. They also assume the elastic response of the solid is *quasistatic* (introducing errors of order the sound crossing time over the gravitational wave period,  $\sim 10^{-3}$ ) and that heat diffuses slowly so the elastic response of the solid to the imposed pressure profile is *adiabatic* (introducing errors of order the diffusion length over the beam size, or  $\sim 0.3 \text{ mm}/10 \text{ cm} \sim 3 \times 10^{-3}$ ).

<sup>3</sup> The mirrors considered in this paper have characteristic dimension of order  $H \sim 10 \text{ cm}$ . Thus, the sound crossing time is of order  $H/c_s \sim H/\sqrt{E/\rho} \sim 10^{-5} \text{ sec}$ . Since the body responds elastically to imposed forces on times of order a few sound-crossing times, the elastic response to a force which is imposed at frequency  $\sim 100\text{Hz}$  is effectively instantaneous. Equivalently, the same conclusion follows because the gravitational wave frequency is far below the frequency of any resonance of the test mass.

2. *Static pressure on mirror face*: An equal and opposite net force  $-F_o\hat{z}$  acts on the mirror face, with a distribution  $P(r)$  proportional to the beam intensity profile. As a result, the displacement field  $y^a$  must satisfy

$$T_{ab}(r, z=0)\hat{z}^b = -F_oP(r)\hat{z}_a, \quad (10c)$$

where the mirror's front (reflecting) surface is at  $z=0$  and where the mirror lies below  $z=0$ .

3. *Break translation symmetry*: Finally, translation symmetry must be broken (i.e. so numerical simulations converge to a unique solution). To break translation symmetry, we fix “the location” of the mirror, where that location is determined as the average location of points in a set  $\mathcal{R}$ . Therefore, to specify a unique solution, we require the displacement field  $y^a$  satisfy

$$\langle y^a \rangle_{\mathcal{R}} = 0 \quad (10d)$$

where  $\mathcal{R}$  is some arbitrary nonempty set and  $\langle \cdot \rangle_{\mathcal{R}}$  denotes the average over  $\mathcal{R}$ .

[This quasistatic approximation to  $I_A$  and the overall thermoelastic power spectrum [Eq. (7)] involves errors only of order  $10^{-3}$  relative to the general Liu-Thorne expression (9) for  $I_A$  [12]; cf. footnotes 2 and 3, or Appendix C.]

### C. Propagation, the eigencondition, and diffraction losses

In the previous two sections, we described mesa beams and the technique by which one can determine, given a beam and four mirrors that support that beam (two identical ITMs and two identical ETMs), the thermoelastic noise an interferometer using those mirrors and beams would experience. But not all combinations of mesa beams and mirrors satisfy advanced LIGO design constraints; the advanced LIGO design specifications require each arm cavity have low diffraction losses per bounce (10ppm).

In this section, we describe how the diffraction losses can be precisely computed [Eq. (15)] and estimated [the clipping approximation, Eq. (16)]. Using the diffraction losses, one can then find combinations of mesa beams and mirrors which produce low diffraction losses per bounce.

Our analysis proceeds by describing in general terms the propagation of light in an arm cavity, focusing in particular on eigenmodes and their loss per round trip. In the process of justifying our simple estimate of diffraction loss, the clipping approximation [Eq. (16)], we will review the definitions and properties of eigenmodes of the arm cavity. This review establishes notation and conventions for our presentation of optical perturbation theory, as discussed in Sec. IV.

### 1. Principles of paraxial optics

The light in LIGO arm cavities is well-described by the paraxial approximation. In this section, primarily to establish notation conventions, we briefly review the propagation of light under the paraxial approximation. A detailed description of the relevant physics can be found in standard references.<sup>4</sup> Briefly, in this approximation, we can completely describe the state of the wave by the wavelength  $\lambda$  of the light used and the values of the wave amplitude on some fixed plane  $z=\text{constant}$  (i.e. transverse to the optic axis) and at some time  $t$  (cf. [14]). The values at any causally-related later combination  $t', z'$ —which must be separated from the transverse plane  $z$  at time  $t$  by a light ray (i.e.  $t' - t = |z - z'|/c$ , mod reflections)—can be deduced by applying the appropriate linear functional to these states.

For example, we could characterize the optical state by the value of the electric field on some plane  $z$ .<sup>5</sup> We would then relate the field at any other plane and at any other time to our initial state via the linear operation

$$E(\vec{r}', z', t') = \int d^2r U(\vec{r}', z'; \vec{r}, z) E(\vec{r}, z, t),$$

cf. Eq. (1). For compactness and clarity, we employ a quantum-mechanics-motivated notation,<sup>6</sup> in which the integrals are suppressed and the operation above is denoted by [cf. Eq. (2)]

$$E(z', t') = U(z', z) E(z, t).$$

By way of example, the following are kernels of integral operators which describe free propagation down a length  $L$ ; reflection off a mirror of height  $h_{1,2}$ ; and a “window” that cuts out all light outside a radius  $r = R_{1,2}$ , respectively:

$$G_L(\vec{r}, \vec{r}') \equiv -i \frac{k}{2\pi L} \exp i \left[ \frac{(\vec{r} - \vec{r}')^2}{2L/k} + kL \right] \quad (11a)$$

$$G_{1,2}(\vec{r}, \vec{r}') \equiv -\delta(\vec{r} - \vec{r}') \exp[-2ik h_{1,2}(r)] \quad (11b)$$

$$T_{1,2}(\vec{r}, \vec{r}') \equiv \delta(\vec{r} - \vec{r}') \Theta(R_{1,2} - r) \quad (11c)$$

where  $\Theta(x)$  is a step function equal to 1 when  $x > 0$  and 0 otherwise, and where the negative sign in  $G_1$  arises because of boundary conditions on the electric field at a perfectly reflecting surface; cf. [14, 15, 16], and other

<sup>4</sup> For a more pedagogical and yet brief presentation, we recommend Blandford and Thorne's treatment [14]. Other pedagogical (and technical) treatments can be found in many laser physics books, e.g., [15, 16, 17, 18]. We also recommend the collection of original research articles on laser and resonator physics compiled by Barnes [19].

<sup>5</sup> We limit attention to a single polarization, e.g., the polarization excited by LIGO.

<sup>6</sup> Most quantum mechanics textbooks written over the past half-century (e.g. [8, 9, 10]) have adopted a similar operator notation.

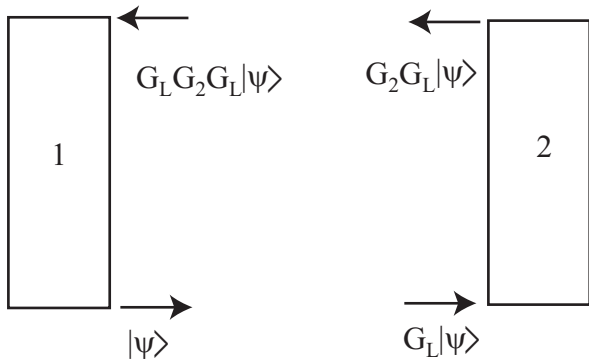


FIG. 3: This figure demonstrates how propagation operators described in Eq. (11) are used to evolve the field from one plane of constant  $z$  to another. For brevity, the operators  $T_1$  and  $T_2$ , which allow for the finite extent of the mirrors' surfaces, have been omitted in this figure.

previously noted references on paraxial optics for further details.

These propagation operations can be combined to generate more complicated processes. For example, while  $G_1$  describes reflection off an *infinite* mirror of height  $h_1$ ,  $G_1 T_1$  describes the reflection of light off a *finite* mirror of height  $h_1$  and radius  $R_1$ .

### 2. Describing paraxial propagation through an arm cavity

When we have an arm cavity bounded by two cylindrical mirrors separated by a length  $L$ , of cylinder radius  $R_{1,2}$  and surface heights  $h_{1,2}$  respectively, we can use the above propagators [Eq. (11)] to describe the free, un-driven propagation of light within the arm cavity<sup>7</sup>. For example, as we demonstrate graphically in Fig. 3, we can express the field at the surface of mirror 1—specifically, the field for light heading *away* from the mirror surface—at time  $t + 2L/c$  in terms of the field at that surface at time  $t$  as follows:

$$u(t + 2L/c) = G_1 T_1 G_L G_2 T_2 G_L u(t) \quad (12)$$

for the operators on the right side as given in Eq. (11) and for  $|u\rangle$  denoting some polarization of the electric field.

We are in particular interested in eigenmodes—that is, states  $u$  so the beam returns proportional to itself:

$$\eta e^{2ikL} u = G_1 T_1 G_L G_2 T_2 G_L u \quad (13)$$

for some  $\eta$ . [We factor the phase  $e^{2ikL}$  out of  $\eta$  to eliminate the effect of the phase factor  $e^{ikL}$  present in

the operator  $G_L$ .] These eigenmodes are *resonant* when  $\eta e^{2ikL}$  is *real* and positive. The arm cavity length  $L$  and wavevector  $k$  are tuned so one state, the *ground state*  $u_o$ , is resonant; in this case,  $\eta_o$ ,  $k$ , and  $L$  satisfy

$$\text{Arg} [\eta_o e^{2ikL}] = 0. \quad (14)$$

The mesa beam [Eq. (5)] is designed specifically to be one of the eigenmodes of the Mexican-hat mirrors [Eq. (6)] when the mirrors are infinite (i.e.  $T_1 = T_2 = \mathbf{1}$ ), and when the cavity length is properly tuned to admit it. When the mirrors are finite, the true eigenmodes of an arm cavity (be it bounded by spherical or Mexican-hat mirrors) will have a slightly different shape than the shape supported by infinite mirrors. Further, the eigenvalue of the arm cavity  $\eta$  will no longer be of unit magnitude (i.e.  $|\eta| < 1$ ).

### 3. Diffraction losses: Exactly

From Eqs. (12) and (13), we know that when the initial optical state is an eigenmode, the optical state after  $n$  round trips decays as measured by its norm, which evolves as  $\|u(t + n2L/c)\| = |\eta|^n \|u(t)\|$ . Thus, if  $|\eta| < 1$  the magnitude of  $u$  (i.e. the  $L^2$  norm of  $u$ ) decreases with each round trip.

Since our model above only permits losses from diffraction, and since the power in the cavity is proportional to  $\int d^2r |u|^2$  (i.e. the  $L^2$  norm of  $u$ , squared), the following quantity is the diffraction loss per round trip:

$$\mathcal{L}_{\text{net}} = 1 - |\eta|^2. \quad (15)$$

When the two mirrors are identical, as is our case, we can subdivide the loss in two, to obtain a meaningful diffraction loss “per bounce”.

We can therefore extract from numerical solutions to Eq. (13) (cf. Sec. VB) the magnitude of  $\eta$  and, by the above expression [Eq. (15)], deduce the mesa-beam diffraction losses in the presence of finite mirrors. We do *not*, however, use this method in this paper.

### 4. Diffraction losses: The clipping approximation

In practice the exact expression for the diffraction losses given above [Eq. (15)] is slow to evaluate, because we must solve for fine details of the eigenequation for each mirror size  $R_{1,2}$  of interest. To obtain a rough estimate of the diffraction losses, usually accurate to a factor of order unity, we will often use instead the clipping approximation.

The clipping approximation estimates diffraction losses by assuming the beam is not significantly changed by those losses; the beam has to a good approximation the same shape as it would have in the presence of infinite mirrors. Assuming the beam profile is known, we then directly compute the losses by determining the power lost

<sup>7</sup> The description of an arm cavity driven by a source laser adds only a straightforward inhomogeneous term to our discussion; the eigenmodes of the homogeneous term are as always in such problems of paramount importance.



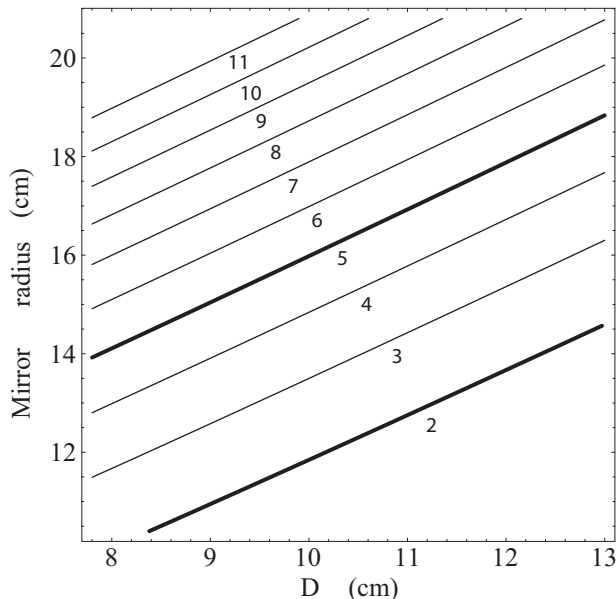


FIG. 4: A contour plot of the ( $\log_{10}$  of the) diffraction losses of the mesa beam [Eqs. (B1) with  $\bar{z} = L/2$ , i.e. (B3)] according to the clipping approximation [Eq. (16)], as a function of mirror radius  $R$  and averaging scale  $D$ . Solid curves indicate losses  $10^{-n}$  for  $n = 2, 3, \dots, 11$ . The two heavy solid curves correspond to  $n = 2$  and  $n = 5$ ; these two curves have special significance to LIGO design (they determine the maximum value of losses off the back and front faces of an ITM, per bounce; cf. Sec. IID).

off the edges of finite mirrors on each reflection. Specifically, we assert  $\mathcal{L}_{\text{net}} \approx \mathcal{L}_{\text{clip}}$ , with

$$\mathcal{L}_{\text{clip}} = \mathcal{L}_1 + \mathcal{L}_2 \quad (16a)$$

$$\mathcal{L}_1 = |(1 - T_1)u_o|^2 = \int_{r>R_1} |u_o|^2 d^2r \quad (16b)$$

$$\mathcal{L}_2 = |(1 - T_2)G_L u_o|^2 = \int_{r>R_1} |G_L u_o|^2 d^2r \quad (16c)$$

where  $u_o$  is an eigensolution to the propagation equation [Eq. (13)] computed assuming infinite mirrors.

5. *Diffraction losses of the ideal mesa beam, computed via the clipping approximation and corrected to estimate the true diffraction losses*

In this paper, we approximate the diffraction losses of the mesa beam resonating between two identical Mexican-hat mirrors by the clipping approximation [Eq. (16)] applied to the mesa beam [Eq. (5)]. These losses are shown in Fig. (4).

The true diffraction losses per bounce generally differ from the estimates of clipping approximation. For example, for a  $D = 4b$  mesa beam resonating between  $R = 16$  cm cylindrical mirrors, the true diffraction losses are about 18.5 ppm, while the clipping approximation

estimates diffraction losses of 21 ppm. Based on this good agreement, in this paper we assumed the true diffraction losses were well-approximated by the clipping-approximation estimate, with relative errors of order a factor 1.2.

#### D. Advanced LIGO design constraints

The advanced LIGO interferometers are composites of many interrelated systems; each component of that system has been designed making assumptions about the other components. In particular, the advanced LIGO interferometers require (roughly) the following constraints on mirror and beam designs:

1. *Mirror mass of 40kg*: We consider only 40kg test-mass mirrors, because the present advanced LIGO design for the suspension and seismic isolation system requires 40kg mirrors. [Also, the advanced LIGO suspension system cannot support heavier mirrors (Phil Willems, private communication)].<sup>8</sup>
2. *Mirror front radius limited by arm-cavity diffraction losses*: We consider only combinations of mirror front face radius  $R$  and beam size (e.g. if mesa beams are used,  $D$ ) which have diffraction losses equal<sup>9</sup> to 10 parts per million (ppm).<sup>10</sup>
3. *Mirror back radius limited by power-recycling-cavity diffraction losses*: Finally, we consider test-mass mirrors whose back face is sufficiently large that light entering the arm cavity through the back face loses at most 1 percent (i.e. 10,000ppm) of the input power.<sup>11</sup> When evaluating this constraint, we assume the input light is in the same state as the arm cavity light (i.e. in a cavity eigenmode).

<sup>8</sup> The support system could hold up lighter mirrors. However, thermoelastic noise decreases as the mirrors and beams are increased in size (in equal proportions). We therefore limit attention to the most massive possible mirrors.

<sup>9</sup> The advanced LIGO design could accept mirrors with lower losses. However, since thermoelastic noise decreases (as a general rule) when the beam radius increases, we limited attention to the largest possible beams.

<sup>10</sup> This constraint is required to keep the diffraction losses bounded by a reasonable portion of the total loss. Specifically, for the baseline design there is 125 W of input power to the interferometer and 830 kW of circulating power in each arm cavity. The 10 ppm of diffraction loss per bounce results in a diffraction power loss in the arm cavities of  $4 \times 10\text{ppm} \times 830\text{kW} = 33$  W, which is 25 per cent of the 125 W of input light, a reasonable value.

<sup>11</sup> As with the constraint involving the front face size (cf. footnote 10), this constraint is required to keep the diffraction losses bounded by a reasonable proportion of the total loss. Specifically, for the baseline design the power impinging on each ITM is 1.05 kW, so one per cent diffraction loss (i.e. 10,000ppm) corresponds to losing  $2 \times 0.01 \times 1.05\text{kW} = 21$  W at the ITM input, which is 17 per cent of the 125 W total laser power.



[This constraint only matters for noncylindrical mirrors (i.e. frustums) with a relatively small back face size; for cylindrical mirrors, it holds automatically.]

### E. Summary: Exploring mesa-beam arm cavity configurations

To summarize, we design and evaluate new mesa-beam interferometer configurations by the following process:

1. *Pick a configuration:* We (i) select two axisymmetric mirrors (i.e. cylinders or frustums) which have the *same* front face radius and (ii) select some value  $D$ . We shape the mirror faces [Eq. (6)] and tune the length of the arm cavity [Eq. (14)] so the ground state eigenmode of that cavity—the eigenmode which is approximately a mesa beam with length scale  $D$ —is resonant.
2. *Check that the configuration satisfies the advanced LIGO design constraints:* If (i) the mirrors masses are not equal to 40 kg, if (ii) the physical diffraction losses in the arm cavity are greater than 10 ppm per bounce [Eq. (15)], or if (iii) the diffraction losses for input light are greater than one percent, then we stop and try again: the configuration does not satisfy the advanced LIGO design constraints described in Sec. IID. [In this paper, we use only the clipping approximation, Eq. (16), to estimate diffraction losses.]
3. *Evaluate the thermoelastic noise of this configuration:* We finally evaluate the noise integrals  $I_1$  and  $I_2$  for each of the two arm-cavity mirrors [Eqs. (9) and (10)], using as beam pressure profile the (normalized) beam intensity profile [Eq. (5)]:<sup>12</sup>

$$P(r) = |u_{\text{mesa}}(r, D)|^2. \quad (17)$$

[Section V A will describe in detail precisely how we evaluated the two thermoelastic noise integrals.]

These thermoelastic noise integrals then determine [via Eq. (7)] the overall thermoelastic noise of an interferometer using two identical arm cavities, where each cavity consists of this particular mirror and beam configuration.

## III. DRIVING A MESA-BEAM ARM CAVITY WITH A GAUSSIAN BEAM

Ideally, a mesa-beam arm cavity would be driven by light already in the mesa-beam state. But if the optics required to generate mesa-beam inputs are unavailable or too inconvenient, Gaussian beams—generated by conventional optics—can be used to drive the arm cavities. With the proper choice of Gaussian, the arm cavity behaves almost as if the ideal mesa beam was used.

In the remainder of this paper, as in the mesa-beam interferometer paper (MBI) [4], we shall assume properly-chosen Gaussian beams are used to drive the interferometer.

In her companion paper [6], Erika D’Ambrosio provides a comprehensive analytic and numerical discussion of Gaussian beams driving mesa-beam cavities [cf., e.g., ED’A Eq. (3)]. In this section, we briefly summarize some of her results on mesa-beam cavities driven by gaussian beams.

### A. Beam and cavity used in this section

#### 1. Fiducial mesa-beam cavity

Rather than study all possible interferometer configurations (i.e. all possible mirror and beam sizes), we select a single *fiducial* mesa-beam arm cavity: the cylindrical mirrors have front face size 16 cm and the mesa beams have  $D = 4b = 10.4$  cm, where  $b = \sqrt{\lambda L}/2\pi = 2.60$  cm (and where  $\lambda = 1.064\mu\text{m}$  and  $L = 4\text{km}$  are the light wavelength and arm length) [cf. MBI Sec. IV A 2]. This fiducial arm cavity has diffraction loss 18 ppm.<sup>13</sup>

We also assume the mirrors bounding the arm cavity—both the input test mass (ITM) and end test mass (ETM)—have no intrinsic losses, except for diffraction losses (which we treat separately). Specifically, we assume the ETM is perfectly reflecting, and assume the ITM has power transmissivity  $t_{\text{I}}^2 = 0.005$  [1]. Thus, our power reflection and transmission coefficients for the ITM and ETM are

$$\begin{aligned} r_{\text{I}}^2 &= 0.995, & t_{\text{I}}^2 &= 0.005; \\ r_{\text{E}}^2 &= 1.0, & t_{\text{E}}^2 &= 0. \end{aligned} \quad (18)$$

[This same fiducial cavity will appear frequently elsewhere; for example, we explore perturbations of this particular fiducial cavity when exploring the sensitivity of the interferometer to tilt.]

<sup>12</sup> Ideally, we *should* use as beam intensity profile the true eigenstate appropriate to two *finite* mirrors, as obtained by solving Eq. (13). However, because diffraction losses are low, the eigenstate for finite mirrors is very well approximated by the eigenstate for infinite mirrors; and the latter is the mesa-beam amplitude  $u_{\text{mesa}}$ .

<sup>13</sup> While not *quite* appropriate—the diffraction losses are slightly larger than the advanced LIGO design cutoff of 10 ppm [1]—this fiducial design is sufficiently similar to acceptable advanced LIGO designs.

## 2. Gaussian beam used to drive the fiducial arm cavity

As described in MBI Sec. IV B, this fiducial arm cavity will be driven by a Gaussian beam of form given in MBI Eq. (2.8), with Gaussian beam radius  $r_{od} = 6.92\text{cm}$ . As in MBI, we denote this state by  $|u_d\rangle$ . This state has overlap

$$\gamma_o^2 \equiv |\langle u_d | u_o \rangle|^2 = 0.940 \quad (19)$$

with the arm cavity's ground state  $u_o$  [cf. MBI Eq. (4.2)]. [Erika D'Ambrosio has found that this particular Gaussian beam gives the largest possible overlap with our fiducial beam; cf. ED'A Eq. (3).]

Strictly speaking, we use a Gaussian state  $|u_d\rangle$  which is shifted by precisely the phase offset necessary to make  $\gamma_o$  real and positive; therefore,

$$\gamma_o = \sqrt{0.940} = 0.970. \quad (20)$$

## B. Operation of fiducial cavity when driven by a Gaussian beam

Equation (19) implies a fraction 0.94 of the (gaussian) driving-beam light will enter the Mexican-hat-mirrored cavity; the remaining 6 percent will be reflected. The fraction of the light that enters the cavity is amplified (due to resonant interaction with the bounding cavity mirrors), but eventually leaks back out the same way it entered (minus that fraction lost through diffraction losses). The combination of the 6 percent reflected light and 94 percent transmitted light (modulo losses) then returns back towards the beamsplitter.

This small section provides a more quantitative view of this entire process.

### 1. Decomposing light along the cavity eigenstates

The transmission and reflection processes are best understood in terms of the resonant eigenstate of the cavity. We therefore rewrite the driving beam in terms of a projection along and perpendicular to the ground state:

$$\begin{aligned} |u_d\rangle &= \mathcal{P}_o |u_d\rangle + (1 - \mathcal{P}_o) |u_d\rangle \\ &= \gamma_o |u_o\rangle + (1 - \mathcal{P}_o) |u_d\rangle \end{aligned} \quad (21)$$

where the projection operator  $\mathcal{P}_o$  is defined so  $\mathcal{P}_o v = |u_o\rangle \langle u_o | v \rangle$  for any state  $v$ , i.e.

$$\mathcal{P}_o \equiv |u_o\rangle \langle u_o|, \quad (22)$$

and where  $\gamma_o$  is defined by (cf. Sec. III A 2)

$$\gamma_o \equiv \langle u_o | u_d \rangle; \quad (23)$$

the phase of  $u_d$  has been designed so the unperturbed  $\gamma_o$  is real. Since the input state  $u_d$  is normalized,

$$\|\mathcal{P}_o u_d\|^2 + \|(1 - \mathcal{P}_o) u_d\|^2 = \|u_d\|^2 = 1. \quad (24)$$

The portion  $\gamma_o u_o$  of the driving field excites the mesa-beam cavity, while the portion  $(1 - \mathcal{P}_o) u_d$  cannot resonate and thus gets fully reflected off the input test mass (ITM).

### 2. Amplification of light entering cavity

A fraction  $\gamma_o^2$  of the light power enters the arm cavity, resonates, and is amplified by a factor

$$\frac{1 + r_I}{1 - r_I} \left( 1 - \frac{2\mathcal{L}_o}{1 - r_I} \right) \quad (25)$$

within the arm cavity,<sup>14</sup> where  $\mathcal{L}_o$  denotes the diffraction losses per bounce for the ground state of the arm cavity. Therefore, relative to the overall input power, the light in the arm cavity is amplified by a factor

$$\mathcal{G}_{\text{anal}} = \gamma_o^2 \frac{1 + r_I}{1 - r_I} \left( 1 - \frac{2\mathcal{L}_o}{1 - r_I} \right) \approx 737. \quad (26)$$

[While the term  $\mathcal{L}_o/(1 - r_I)$  is very small in this case and can be ignored, we provide the entire expression now for use in Sections IV and VII, when we study the effect of mirror perturbations on the cavity gain.]

### 3. Output: Transmission of light out of cavity, and recombination with reflected light

The cavity's output light is the combination of light reflected at the ITM (which does not enter the cavity) and light exiting the arm cavity through the ITM. After some algebra (cf. [6]),<sup>15</sup> we find that given a driving beam  $u_d$  decomposed according to Eq. (21) the reflected light  $u_r$  is in the state

$$\begin{aligned} |u_r\rangle &= \mathcal{P}_o |u_d\rangle - (1 - \mathcal{P}_o) |u_d\rangle \\ &= (2\mathcal{P}_o - 1) |u_d\rangle. \end{aligned} \quad (27)$$

where for simplicity we have ignored the (small) effects of diffraction losses on the light that resonates in the cavity.

<sup>14</sup> The second (unnumbered) equation in D'Ambrosio [6] gives the transmitted field through the arm cavity. Dividing this by the second mirror transmissivity, squaring it to get an expression for beam power, and then specializing to  $r_2 = 1$  and  $r_1 = r_I$ , we obtain the first factor in Eq. (25). The second factor arises when losses are properly taken into account on each bounce.

<sup>15</sup> The portion of the beam amplitude proportional to the arm cavity ground state enters the arm cavity and resonates. It therefore exits that the arm cavity with the same phase it enters. On the other hand, the rest of the light experiences nearly perfect destructive interference. For the rest of the light, the arm cavity acts like a perfectly reflecting mirror, so that portion of the light amplitude exits the arm cavity with the opposite phase than it entered with. For a more precise demonstration of this effect, see for example the first equation in D'Ambrosio [6] with  $r_2 = 1$ ,  $t_1 = t_I$  and  $r_1 = r_I$ , and both exponential factors unity.

#### IV. EFFECT OF MIRROR PERTURBATIONS ON ARM CAVITIES AND THE INTERFEROMETER

In Section II, we described how to design an idealized mesa-beam arm cavity and to evaluate the thermoelastic noise associated with such a design.

In this section, we shall describe in extremely general terms how one can use perturbation theory to study the influence of defects on a single ideal (i.e. lossless) arm cavity. We make no reference to the specific details of the cavity used, save that—for technical convenience—we limit attention in our perturbation theory to a system with two identical, infinite mirrors. [Recall the canonical mesa beams, as defined in Sec. II A, are designed for symmetric cavities.] Naturally the methods for perturbing arbitrary mirrors bear considerable similarity to methods for perturbing purely spherical mirrors. Many explicit tools and concepts carry over with little change to our more generic approach.

Specifically, in Sec. IV A we introduce the orthonormal basis set of solutions we shall use to construct the perturbation theory expansion. Then, in Sec. IV B, we list the explicit second-order perturbation expansions we use to deduce the effect of mirror defects upon the optical state of the cavity. Finally, in Sec. IV C, we describe how changes in the optical state of the cavity influence other quantities that can be deduced from that state, such as the cavity diffraction losses [Eq. (16)] and the thermoelastic noise integrals  $I_A$  [Eq. (9)].

##### A. Basis states for perturbation theory

We will use perturbation theory to analyze the effect of small changes in the arm cavity mirrors on the solutions to the eigenequation (13). To construct perturbation theory expansions by methods similar to those used in quantum mechanics (cf., e.g., [8, 9, 10]), we *prefer* to use as a basis for the perturbation expansion the eigenmodes of the initial equation [Eq. (13)].<sup>16</sup> Fortunately, as shown in Appendix D, so long as the two mirrors are identical and infinite, the set of eigenmodes of Eq. (13) are a complete, orthogonal set, independent of the mirror shape.

At this point, we could introduce basis states (and notation for basis states) which are defined as eigensolutions to Eq. (13). For technical reasons—our methods simplify practical evaluation of the perturbation equation<sup>17</sup>—we

prefer instead to use a basis designed to simplify “half” (i.e. a square root of) the round-trip operator, with a certain phase factor removed. In other words, we use as basis states the eigensolutions  $|p\rangle$ ,  $\lambda_p$  to the equation

$$\lambda_p |p\rangle = e^{-ikL} G_1 G_L |p\rangle \quad (28)$$

where  $|p\rangle$  is some state and  $p$  denotes some index over all basis states. [By an argument following that given in Appendix D, this equation admits a complete set of orthogonal solutions  $|p\rangle$ .] These states correspond directly to solutions to the full eigenequation. Explicitly, if we insert a solution  $|p\rangle$  to Eq. (28) into the eigenequation [Eq. (13)], we immediately conclude that  $|p\rangle$  is also an eigensolution of Eq. (13), with eigenvalue

$$\eta_p = \lambda_p^2. \quad (29)$$

##### B. Effect of perturbations on light in the arm cavities

When the mirror shapes  $h_{1,2}$  are deformed, the light propagating in the cavity changes. Given a basis of states and a specific problem to perturb [Eq. (13)], we employ conventional techniques from quantum mechanics (cf., e.g., [8, 9, 10]) to compute that change.

###### 1. Results of perturbation expansion

Using conventional quantum-mechanics-style techniques (cf., e.g., [8, 9, 10]), but note the operator we perturb is unitary rather than hermitian), we can devise a perturbative expansion for the cavity ground state eigenvalue  $\eta'_o$  and state  $u'_o$  in powers of the height perturbation  $\delta_2$ . The derivations of the sometimes-long expressions noted here are provided in Appendix E.

For simplicity, we provide perturbation theory expansions only to second order, and only to describe the effects due to changes in the height of one mirror (i.e.  $h_2$  of mirror 2) by an amount  $\delta h$ . To express these changes in height in dimensionless form, we introduce the variable  $\delta_2$ :

$$\delta_2 \equiv 2k\delta h_2. \quad (30)$$

*Change in eigenvalue:* The eigenvalue  $\eta_o$  of the ground

<sup>16</sup> Actually, as Erika D’Ambrosio has frequently reminded us, we can construct perturbation theory just as well in the more general case, by using a dual basis. See, for example, Appendix A of D’Ambrosio [6].

<sup>17</sup> On the one hand, by removing the common factor  $\exp(ikL)$  present in  $G_L$ , we produce a naturally dimensionless eigenvalue problem (as  $k$  and  $L$  enter only through the single length pa-

rameter  $b$ ). On the other hand, by focusing on “half” of the propagator rather than a round-trip operator, we can easily deduce the relationship between the fields at the two ends of the cavity. The latter proves helpful, because we will study perturbations of the mirror at one end of the cavity (end 2), yet represent the state of the cavity field by its values on the other end (end 1).

state  $|u_o\rangle = |0\rangle$  changes as

$$\eta'_o = \eta_o \left( 1 - i \langle 0 | \delta_2 | 0 \rangle - \frac{\langle 0 | \delta_2^2 | 0 \rangle}{2} - \sum_{k \neq 0} \frac{\eta_k |\langle 0 | \delta_2 | k \rangle|^2}{\eta_o - \eta_k} \right) \quad (31)$$

*Change in eigenstate:* When we construct the perturbation theory expansion to second order, we find the ground state changes according to an expression of the form

$$|u'_{o,\text{pt}}\rangle \approx |0\rangle + |\psi^{(1)}\rangle + |\psi^{(2)}\rangle. \quad (32a)$$

In this expression,  $\psi^{(1)}$  and  $\psi^{(2)}$  denote those terms first- and second-order in  $\delta_2$  in the perturbation expansion, respectively. To be explicit, when we perform the perturbation theory expansion [details of which are provided in Appendix E], we find

$$|\psi^{(1)}\rangle = \sum_{k \neq 0} -\frac{i\lambda_o\lambda_k}{\eta_o - \eta_k} |k\rangle \langle k | \delta_2 | 0 \rangle, \quad (32b)$$

$$|\psi^{(2)}\rangle = \sum_{k \neq 0} |k\rangle \frac{\lambda_o\lambda_k}{\eta_o - \eta_k} \left[ -\frac{1}{2} \langle k | \delta_2^2 | 0 \rangle + \frac{\eta_o}{\eta_o - \eta_k} \langle k | \delta_2 | 0 \rangle \langle 0 | \delta_2 | 0 \rangle - \sum_{p \neq 0} \frac{\eta_p}{\eta_o - \eta_p} \langle k | \delta_2 | p \rangle \langle p | \delta_2 | 0 \rangle \right]. \quad (32c)$$

By construction  $|\psi^{(1)}\rangle$  and  $|\psi^{(2)}\rangle$  are orthogonal to the unperturbed ground state  $|0\rangle$ . As a result, this expression (32) for  $|\psi'\rangle$  is *not* normalized: we find, working to second order, that the norm of  $|u'_{o,\text{pt}}\rangle$  is

$$\langle u'_{o,\text{pt}} | u'_{o,\text{pt}} \rangle \approx 1 + \|\psi^{(1)}\|^2 + \mathcal{O}(\delta_2^3). \quad (33)$$

where we use the shorthand  $\|\psi\|^2 \equiv \langle \psi | \psi \rangle$ . Therefore, the physically appropriate normalized perturbed state  $|u'_o\rangle$  is given by the expression

$$\begin{aligned} |u'_o\rangle &\approx \frac{1}{\sqrt{1 + \|\psi^{(1)}\|^2}} \left( |0\rangle + |\psi^{(1)}\rangle + |\psi^{(2)}\rangle \right) \\ &= |0\rangle + |\psi^{(1)}\rangle + \left( |\psi^{(2)}\rangle - \frac{\|\psi^{(1)}\|^2}{2} |0\rangle \right) + \mathcal{O}(\delta_2^3). \end{aligned} \quad (34)$$

## 2. Estimating convergence of perturbation expansion

Perturbation theory is only effective when higher order terms provide only a small correction to lower order terms. To test the convergence of the series, we compare the magnitudes of the first two perturbative corrections. When  $\|\psi^{(2)}\|/\|\psi^{(1)}\| \ll 1$ , we believe the series converges and our expressions should be effective.

## C. Implications of change in optical state for other quantities

In the previous section, we described the effect of perturbations  $\delta h_{1,2}$  on light propagating in a single Fabry-Perot arm. These perturbations cause the beam shape incident on the two mirrors to change, generally in a different way at each mirror. Therefore, quantities that depend on the state of the beam at each mirror, such as the diffraction losses and thermoelastic noise integrals  $I_A$ ,

also change. In this section, we loosely describe how the lowest order effect of these changes can be characterized.

### 1. Change in diffraction losses under perturbation of one mirror

Unfortunately, a systematic treatment of diffraction losses within the context of perturbation theory proves very tricky, not the least because we must represent both the height change and the effect of finite mirror size as perturbations, then use many states to insure the perturbation theory expansion converges properly for the effects of diffraction.

Rather than perform a truly accurate, well-motivated computation, we will in this paper loosely estimate diffraction losses by the clipping approximation applied to the perturbed beam state. By way of example, we can estimate the diffraction losses produced during a single reflection off of mirror 1 or off mirror 2 in the presence of a perturbation of mirror 2 by expanding the appropriate clipping approximation estimate  $\mathcal{L}_1$  or  $\mathcal{L}_2$  [cf. Eq. (16)]:

$$\mathcal{L}_1 \approx \langle u | O_1 | u \rangle, \quad (35a)$$

$$\mathcal{L}_2 \approx \langle G_L u | O_2 | G_L u \rangle, \quad (35b)$$

$$O_1 \equiv 1 - T_1, \quad (35c)$$

$$O_2 \equiv 1 - T_2. \quad (35d)$$

To be explicit, we can expand the clipping-approximation estimate for  $\mathcal{L}_1$  to second order in  $\delta_2$  as

$$\begin{aligned} \mathcal{L}_1 &\approx \langle 0 | O_1 | 0 \rangle + 2\text{Re} \left( \langle \psi^{(1)} | O_1 | 0 \rangle \right) \\ &+ \langle \psi^{(1)} | O_1 | \psi^{(1)} \rangle - \|\psi^{(1)}\|^2 \langle 0 | O_1 | 0 \rangle \\ &+ 2\text{Re} \left( \langle \psi^{(2)} | O_1 | 0 \rangle \right) + \mathcal{O}(\delta_2^3). \end{aligned} \quad (36)$$

A similar expression is found for  $\mathcal{L}_2$ , with  $O_1$  replaced by  $G_L^\dagger O_2 G_L$ . [Because the beam profile will generally change in different ways at the two ends due to a perturbation localized at only one end, generally  $\mathcal{L}_1 \neq \mathcal{L}_2$ .]

### 2. Change in cavity gain due to perturbations of one mirror

The amount of power resonating in the cavity also changes, in part through modified diffraction losses [Eq. (36)] but also through a change in the resonant ground state of the cavity from  $u_o$  (i.e.  $|0\rangle$ ) to  $u'_o$  [Eq. (34)]. Because the resonant state of the cavity changes, the overlap  $\gamma_o$  changes to  $\gamma'_o$ , which to second order can be approximated by

$$\gamma'_o \equiv \langle u'_o | u_d \rangle = \left( 1 - \frac{\|\psi^{(1)}\|^2}{2} \right) \gamma_o + \gamma_1 \|\psi^{(1)}\| + \gamma_2 \|\psi^{(2)}\|, \quad (37a)$$

where we define

$$\gamma_1 \equiv \langle \psi^{(1)} | u_d \rangle / \|\psi^{(1)}\|, \quad (37b)$$

$$\gamma_2 \equiv \langle \psi^{(2)} | u_d \rangle / \|\psi^{(2)}\|. \quad (37c)$$

To be very specific, we can find the perturbed cavity gain  $\mathcal{G}'_{\text{anal}}$  by evaluating Eq. (26) to second order in  $\delta h_2$ ,

$$\mathcal{G}'_{\text{anal}} = \gamma_o'^2 \frac{1+r_I}{1-r_I} \left( 1 - \frac{\mathcal{L}'_1 + \mathcal{L}'_2}{1-r_I} \right), \quad (38)$$

using Eq. (36) for the perturbed diffraction losses  $\mathcal{L}_1$  and  $\mathcal{L}_2$  and using Eq. (37) for the change in overlap between the perturbed cavity ground state and the driving beam.

[Though we do not write out the resulting second-order expansion in full detail, we will apply these methods to compute to second order the effects of mirror tilt on cavity gain in Sec. VII.]

### 3. Change in dark port power due to perturbations of one mirror

An interferometer consists of two arms. When the beamsplitter recombines the two fields leaving the two arm cavities, the light going out the dark port of the interferometer ( $u_{\text{dp}}$ ) is the interference between the light reflected off the two arms (denoted I and II):

$$u_{\text{dp}} = \frac{1}{\sqrt{2}}(u_{r,\text{II}} - u_{r,\text{I}}). \quad (39)$$

If both cavities are identical, then  $u_{r,\text{II}} = u_{r,\text{I}} = u_r$  for  $u_r$  given by Eq. (28) and no light exits the dark port. If the cavities are perturbed, however, power will generically go out the dark port.

For example, if only cavity II is perturbed, then  $u_{r,\text{II}} = u'$ ,  $u_{r,\text{I}} = u_r$ , and the dark port beam state is

$$\begin{aligned} u_{\text{dp}} &= \frac{1}{\sqrt{2}}(u'_r - u_r) \\ &= \sqrt{2}(\mathcal{P}'_o - \mathcal{P}_o)u_d \\ &= \sqrt{2}(\gamma'_o u'_o - \gamma_o u_o) \\ &= \sqrt{2} \left[ \left( -\gamma_o \|\psi^{(1)}\|^2 + \gamma_1 \|\psi^{(1)}\| + \gamma_2 \|\psi^{(2)}\| \right) |u_o\rangle \right. \\ &\quad \left. + \left( \gamma_o + \gamma_1 \|\psi^{(1)}\| \right) |\psi^{(1)}\rangle \right. \\ &\quad \left. + \gamma_0 |\psi^{(2)}\rangle \right] + O(\delta_2^3). \end{aligned} \quad (40a)$$

where going from the first line to the second we use Eq. (28) [for  $u_r$ ]; from the second to the third we use Eqs. (22) [for  $\mathcal{P}_o$ ] and (23) [for  $\gamma_o$ ]; and from the third to the fourth we use the perturbation expansions (32) [for  $u'_o$ ] and (37) [for  $\gamma'_o$ ].

The dark port power  $P_{\text{dp}}$  (as a relative fraction of interferometer input power, which is twice the input power to each arm cavity) can be expressed as

$$P_{\text{dp}} = \|u_{\text{dp}}\|^2 / 2, \quad (40b)$$

an expression which we shall not expand here.

### 4. Influence of perturbations of one mirror on thermoelastic noise

The thermoelastic noise integrals associated with each mirror (1 and 2) in a given arm cavity both change because the beam profile at each mirror changes. To evaluate those changes, we insert the modified state [Eq. (34)] into the thermoelastic noise integral  $I_A$  [Eq. (9)].

For example, to evaluate the linear-order change in thermoelastic noise at mirror 1, we first take the new normalized intensity profile  $P(r)$  at mirror 1, given by

$$\begin{aligned} P'_1(r) &\equiv |u'_o(r)|^2 \\ &\approx |u(r)|^2 + 2\text{Re} \left( u_o^*(r) \psi^{(1)}(r) \right) + O(\delta_2^2). \end{aligned} \quad (41)$$

Using this new intensity profile, we solve the thermoelastic noise model problem [Eq. (10)] for the expansion  $\Theta'$  and in particular the first-order change in expansion  $\delta\Theta \equiv \Theta' - \Theta$ . Finally, we insert this first order change  $\delta\Theta$  into the expression for  $I_A$  with  $A = 1$ , linearized about the background intensity profile:

$$\delta I_1 = \frac{2}{F_o^2} \int_{V_1} (\nabla_a \Theta) (\nabla^a \delta\Theta) d\text{volume} \quad (42)$$

where  $\Theta$  is the expansion produced by the unperturbed pressure profile  $F_o P$ .

The beam shape at mirror 2 also changes; by a similar construction, we can find its effect on the thermoelastic noise integral  $I_2$ .

## D. Observations which simplify our computations

1. *Symmetry and the influence of first-order changes in state*

The ground-state beam of physical interest is isotropic. As a result, when we perform the computations outlined above, we find only the *axisymmetric* (about the optic axis) part of  $|\psi^{(1)}\rangle$  contributes to first-order changes in the three integral quantities of physical interest (the overlap  $\gamma_o$ ; diffraction losses; and thermoelastic noise).

By way of example, consider the first-order change in thermoelastic noise [Eq. (42)]. Since the unperturbed pressure profile and thus unperturbed expansion ( $\Theta$ ) are isotropic, the above integral couples only to the axisymmetric part of  $\delta\Theta$  and therefore  $\delta P$  and  $\psi^{(1)}$  [cf. Eq. (41)].

Similarly, to lowest order displacement and tilt perturbations have odd parity; therefore, symmetry insures that the first-order change  $\gamma_1$  [Eq. (37)] is zero.

2. *Assuming (roughly) equal contributions from the two mirrors to changes in  $I_A$  and diffraction losses*

The change in mirror shape at mirror 2 produces roughly comparable changes to the beam profile at both ends. To a rough approximation, then, we can assume that the changes in thermoelastic noise and diffraction loss at mirror 2 will be comparable to their changes at mirror 1.

## E. Summary: Using perturbation theory to explore the sensitivity of the arm cavity and interferometer to perturbations

To summarize, we evaluate how sensitive mesa-beam arm cavities and interferometers are to mirror perturbations as follows:

1. *Assume the arm cavity is fiducial:* The perturbation expansions above can be applied to any arbitrary mirror configuration (i.e. to any specific mesa-beam  $D$ ).<sup>18</sup> In principle, we *could* apply perturbation theory to all possible mirror configurations generated in Sec. II. Instead, to avoid repeating computations which should yield nearly identical results, we apply perturbation theory only to the *fiducial* advanced LIGO arm cavity presented in Section III A 1.

2. *Consider only perturbations of one ETM:* Similarly, we change only one end test mass in one arm cavity, rather than apply perturbations to each test-mass mirror.

3. *Compute the eigenmodes of the fiducial arm cavity:* We find the natural eigenmodes of the fiducial arm cavity—and therefore the basis states  $|p\rangle$  in our perturbation expansion—by numerically solving the basis-state eigenequation (28). [The numerical code which solved this integral eigenequation is described in Sec. V B.]

4. *Find how the ground state of arm cavity changes:* Next, we apply the perturbation expansion [Eq. (32)] to find how the ground state of the arm cavity changes when each perturbation of physical interest is applied: tilt, displacement, and mirror figure error. In other words, for each of these perturbations  $\delta h_2$ , we use Eq. (32) to find the first- and second-order corrections  $|\psi^{(1)}\rangle$  and  $|\psi^{(2)}\rangle$  to the state of the cavity.

5. *Determine how the thermoelastic noise integral  $I_A$  for each mirror changes:* Given the changed beam state, we can recompute the thermoelastic noise integral  $I_A$  for each mirror (cf. Sections II and V A), using the perturbed beam state  $u'_o(r)$  and the perturbed beam intensity profile  $P'(r) = |u'_o(r)|^2$ . More directly, the series expansion of thermoelastic noise can be discovered by a series expansion of the thermoelastic noise integral, as sketched (to first order) in Sec. IV C 4.

6. *Describe how the cavity gain and dark port power change:* Finally, given the changed beam state, we can also recompute the arm cavity gain [Eq. (38)] and interferometer dark port power [Eq. (40)] when the ETM of one cavity is perturbed. These two expressions both depend on how the perturbed arm cavity interacts with the driving beam [i.e. on  $\gamma_1$  and  $\gamma_2$ ; cf. Eq. (37)] and on the perturbed arm cavity state itself [i.e. on  $\|\psi^{(1)}\|$  and  $\|\psi^{(2)}\|$ ; cf. Eq. (32)]. Also, the cavity gain depends on how the diffraction losses of the arm cavity change [Eq. (36)].

## V. NUMERICAL IMPLEMENTATIONS OF THE THERMOELASTIC NOISE INTEGRAL, THE OPTICAL EIGENEQUATION, AND OPTICAL PERTURBATION THEORY

In the previous two sections, we described the abstract expressions we must evaluate to design and analyze an arm cavity bounded by Mexican-hat mirrors. In this section, we describe how we implemented and solved those equations.

<sup>18</sup> Our technique assumes the cavity eigenmodes of an arm cavity with finite mirrors are well-approximated by the modes of a cavity with infinite mirrors. Therefore, the only relevant parameter remaining is the mesa-beam averaging scale  $D$ . [This approximation ignores quantities of order the diffraction losses, 10 ppm  $\sim 10^{-5}$ .]

Where independent methods were used to perform a particular computation, we indicate the different techniques used.

### A. Thermoelastic noise for perfect (undeformed) mirrors

To evaluate the thermoelastic noise power spectrum [Eq. (7)], we need to perform two tasks. First, we must solve the elasticity problem described in Eq. (10); then, using the result, we can evaluate the integral  $I_A$ , which enters directly in Eq. (7).

We employed three methods to address these two tasks. The first two methods—a numerical (finite-element) solution and an exact analytic solution—applied only to special circumstances: axisymmetric beam profiles, and cylindrical mirrors. The third method was an approximation based on assuming the mirror to be half-infinite; we used it only as a quick, easy-to-evaluate check on the qualitative behavior of the previous two methods.

#### 1. General approach

We usually solved the elasticity equations (10b)-(10d) using a commercial two-dimensional finite-element code [22]. We chose the region  $\mathcal{R}$  in Eq. (10d) to be one of the mirror faces.<sup>19</sup> [To use a two dimensional code, we limited attention to *axisymmetric* mirrors and pressure profiles.]

The commercial finite-element code we employed gave us the displacement vector  $y^a$ . We then used postprocessing code discussed in Appendix G to evaluate the derivatives and integrals needed in Eq. (9).

#### 2. Special case: cylindrical mirror

Independently, we employed the analytic elasticity solution Liu and Thorne (LT) [12] developed for cylindrical mirrors with axisymmetric pressure profiles imposed on them.

Liu and Thorne constructed a solution to the elasticity equations for a cylinder [Eqs. (10b)-(10d)] which they apply to Eq. (9) to find an explicit expression for the thermoelastic noise produced by gaussian beams on cylindrical mirrors. By replacing a single equation in their expressions, we can convert their solution to one appropriate to *arbitrary* axisymmetric beam intensity profiles.

To be explicit, LT Eq. (44) gives an expression that is precisely  $1/2$  of  $I$  ( $1/2$  because of averaging which we have factored out but which LT retain), in terms of quantities defined in LT Eqs. (35) and (36). To generalize to a generic axisymmetric pressure profile, one need only change LT Eq. (36)—the only equation which involves the specific pressure profile—so that it involves the intensity function  $P(r)$  defined in Eq. (10c) for  $m > 0$ :<sup>20</sup>

$$p_m = \frac{2}{a^2 J_0^2(\zeta_m)} \int_0^a P(r) J_0(\zeta_m r/a) r dr. \quad (43)$$

Here  $a$  is the radius of the cylindrical mirror (denoted  $R$  elsewhere in this paper);  $\zeta_m$  is the  $m$ th zero of  $J_1(x)$ ; and the functions  $J_0$  and  $J_1$  are the zeroth and first order cylindrical Bessel functions. The sum converges rapidly: typically, only a handful of terms in the infinite sum [LT Eq. (45)] are required.

#### 3. Approximate technique: half-infinite mirrors

If the mirror is sufficiently large compared to the imposed pressure profile  $P(r)$ , the elasticity problem we must solve [Eq. (10)] can be well approximated by a solution to a similar problem with the mirror boundary taken to infinity. In this case, as the force density term [Eq. (10c)] goes to zero, we need only solve for the response of a half-infinite (i.e. filling the region  $z < 0$ ) elastic medium to an imposed surface pressure. As described in greater detail in Appendix H, analytic expressions exist for the response, permitting us to find an compact expression for the thermoelastic noise integral. We find

$$I = \left( \frac{(1 + \sigma)(1 - 2\sigma)}{2\pi E} \right)^2 \int d^2 \vec{K} \left| \vec{K} \right| \left| \tilde{P}(\vec{K}) \right|^2 \quad (44)$$

where  $\tilde{P}(\vec{K})$  is the two-dimensional Fourier transform of  $P(\vec{r})$ :

$$\tilde{P}(\vec{K}) \equiv \int d^2 \vec{r} e^{-i\vec{K} \cdot \vec{r}} P(\vec{r}). \quad (45)$$

Recall that  $P(\vec{r})$  is normalized to unity (cf. Sec. II B).

### B. Numerically solving for the resonant optical eigenmodes of a cavity bounded by arbitrary axisymmetric mirrors

To test the validity of the clipping approximation [Eq. (16)] against the exact diffraction losses [Eq. (15)] and to generate the set of basis solutions needed to construct

<sup>19</sup> The code works faster if the region  $\mathcal{R}$  is a point or set of points. However, the code is significantly more susceptible (on physical grounds—the points act like “nails” in the mirror) to small errors in the neighborhood of points, errors that contribute significant erroneous expansion. Therefore, as a practical compromise we chose  $\mathcal{R}$  to be a surface.

<sup>20</sup> The LT coefficient  $p_o$  is independent of the pressure profile shape; it is always  $1/\pi a^2$ .



perturbation theory [Eq. (28)], we must numerically solve for the cavity eigenmodes. In this section, we describe numerically how we converted the cavity eigenmode integral equation into a numerical eigenproblem, which we then solved with standard numerical tools (e.g., Mathematica).

### 1. Setting up the problem to be solved; preliminary analytic simplifications

Rather than solve the eigenequation for a full round trip through a symmetric cavity [Eq. (13) with  $R_1 = R_2$ ], we exploit symmetry and instead study the closely related problem of *half* a round trip through a symmetric cavity. In other words, we plan to diagonalize the basis state eigenequation [Eq. (28)] when that eigenequation is restricted to the space of functions defined on  $R_1 = R_2 \equiv b X_{\max}$ :

$$\lambda |u\rangle = T_1 G_1 G_L T_1 \exp(-ikL) |u\rangle \quad (46)$$

If we write out the appropriate eigenequation for this “half-a-round-trip” operator, making use of the definitions in Eq. (11) and using the dimensionless spatial units  $\vec{X} = \vec{r}/b$ , we find the following integral equation:

$$\lambda \psi(\vec{X}) = \int d^2 X' \mathcal{G}(X; X') \psi(\vec{X}'), \quad (47a)$$

$$\mathcal{G}(\vec{X}; \vec{X}') \equiv \frac{-i}{2\pi} \Theta(X_{\max} - |\vec{X}'|) e^{i \left[ \frac{(\vec{X} - \vec{X}')^2}{2} - \bar{h}(X) \right]} \quad (47b)$$

$$\bar{h} \equiv 2kh. \quad (47c)$$

Here,  $\psi(\vec{X}) = u(\vec{r})/b$  denotes a dimensionless representation of the state  $u$ .

Since the mirror surfaces are (ideally) axisymmetric, the operators above all commute with rotation around to the optic axis. We can therefore mutually diagonalize this operator and the generator of rotations. Therefore, we require  $\psi$  be proportional to  $\exp(im\varphi)$  for some integer  $m$ :

$$\psi(X, \varphi) \equiv \Phi(X) e^{im\varphi}. \quad (48)$$

Substituting in this form for  $\psi$ , we reduce the problem to a series of one-dimensional integral equations, one for each  $|m|$ :

$$\eta \Phi(X) = \int_0^{X_{\max}} \bar{X} d\bar{X} \mathcal{G}_m(X, \bar{X}) \Phi(\bar{X}), \quad (49a)$$

$$\mathcal{G}_m(X, \bar{X}) = -i^{m+1} J_m(X\bar{X}) e^{i \left[ \frac{X^2 + \bar{X}^2}{2} - \bar{h}(X) \right]} \quad (49b)$$

### 2. Method of numerical solution

For each  $m$  of interest, we represent the integral operator on the right side of Eq. (49) as a matrix. For

simplicity, we discretize space in a uniform grid  $X_A = AX_{\max}/(N-1)$  for  $A = 0 \dots N$ , define  $\Phi_A = \Phi(X_A)$  and similarly, and approximate the integral by a simple quadrature rule.<sup>21</sup> Thus, we approximate the integral equation of Eq. (49) by the matrix eigenvalue problem

$$\lambda \Phi_A = \sum_{B=0}^N \frac{X_{\max}^2 B}{(N-1)^2} \mathcal{G}_m(X_A, X_B) \Phi_B \quad (50)$$

This equation can be solved for  $\eta$  and  $\Phi$  by any standard eigensolution package.

### 3. Interpreting and applying the numerical solution

To summarize, to find numerical approximations to eigensolutions  $\psi$  of Eq. (46)—an eigenequation similar to the basis-state eigenequation [Eq. (28)] but for mirrors of finite radius  $R = bX_{\max}$ —we construct and solve the matrix eigenvalue problem (50).

The approximate eigensolutions  $\eta_p$  and  $\Phi$  so obtained provide numerical approximations to the two cavity-eigenproblems of technical interest:

- *Solutions for true cavity eigenmodes:* This method provides us with precisely the numerical cavity modes needed to understand mesa beams in the presence of finite mirrors. [Specifically, eigenmodes and eigenvalues of Eq. (46) are also eigenmodes of Eq. (13).] In particular, we can use the norm  $|\eta|$  to determine the round-trip diffraction losses according to Eq. (15).
- *Solutions for the basis states:* Further, by making the mirrors sufficiently large that diffraction effects can be ignored<sup>22</sup>, solutions to Eq. (46) provide good approximations to solutions to the basis eigenvalue problem [Eq. (28)].

## C. Numerical implementation of perturbation theory

To use perturbation theory exactly [i.e. Eqs. (31) and (32)], one needs an infinite collection of states. In practice, we limited attention to a handful: the lowest-lying ten to twenty for each  $|m| = 0, \dots, 7$ ; more modes were used when the rate of convergence of the perturbation theory expansion suggested more were needed.

<sup>21</sup> We in fact used the equation Eq. (50) as stated. More sophisticated quadrature techniques, such as Gaussian quadrature, offer greater accuracy with fewer points (and hence significantly less computation time).

<sup>22</sup> As a practical matter, we test the quality of our solutions by observing the convergence of the norm  $|\eta|$  as we increase the number of points used to represent the state.

#### D. Numerical exploration of changing diffraction losses

Given the  $\delta h_2$ -induced perturbed beam state  $|\psi\rangle$  at mirror 1, we can compute the (clipping approximation estimate of the) diffraction losses at mirror 1 for a given height perturbation  $\delta h_2$  at mirror 2. Largely, we simply evaluated the integrals (i.e. inner products and norms) required to construct Eq. (36). However, to provide an independent numerical check (i.e. to insure we had no typographical or structural errors), we also evaluated the diffraction losses directly, using the definition Eq. (16), for a sequence of height perturbations  $\delta h(\varepsilon) \equiv \varepsilon \delta h_2$  with  $\varepsilon = 0, 0.1, 0.2, \dots, 1$ ; then fitted a second-degree polynomial to the resulting data points to extract the series coefficients in Eq. (36).

#### E. Numerical investigation of changes in thermoelastic noise when one mirror shape is perturbed

Finally, we can use the known form of  $\psi^{(1)}(r, \varphi)$  [from Eq. (32b)] in the procedure outlined earlier [cf. Eqs. (41) and (42)] to evaluate the first-order change in thermoelastic noise associated with mirror 1 due to changes in the shape of mirror 2.

Specifically, given  $\psi^{(1)}(r, \theta)$ , we use Eq. (41) to find how the pressure profile changes. We then use the first-order change  $\delta P$  to the pressure profile in the LT expression for thermoelastic noise (see Sec. V A 2), linearized about the response to the unperturbed cavity beam intensity  $P$ . [We will not provide the rather lengthy but straightforward linearization of the LT expressions here; any computer-algebra system can easily reproduce the desired expansion.]

### VI. DEPENDENCE OF THERMOELASTIC NOISE ON MIRROR AND BEAM SHAPE

In this section, we explore the dependence of the thermoelastic noise integral  $I_A$  [Eq. (9)] on the various arm cavity parameters available to us: (i) the mirror's dimensions (i.e. cylinder height and radius) and shape (i.e. frustum or cylinder), (ii) the beam size (e.g., the mesa-beam size  $D$ ), and (iii) the type of beam resonating in the arm cavity (i.e. Gaussian or mesa). The thermoelastic noise integral provides a simple way to characterize how the thermoelastic noise power spectrum  $S_h$  [Eq. (7)] of these configurations compares to  $S_h$  for the baseline advanced LIGO configuration ( $S_h^{\text{BL}}$ ):

$$S_h/S_h^{\text{BL}} = I/I_{\text{BL}}, \quad (51)$$

where  $I_{\text{BL}}$  (evaluated below) is the value of the thermoelastic noise integral for the baseline advanced LIGO configuration [Eq. (52)], and where  $I$  is the value of the

thermoelastic noise integral for all four (identical) mirrors in the interferometer.

Specifically, in this section we compare the following types of mirror and beam configurations, all of which satisfy the advanced LIGO design constraints [Section II D]: (i) the baseline advanced LIGO configuration (which uses Gaussian beams and cylindrical mirrors); (ii) an improved baseline configuration (which also uses Gaussian beams and cylindrical mirrors); (iii) configurations with mesa-beam light resonating between identical cylindrical mirrors; and (iv) configurations with mesa-beam light resonating between identical frustum mirrors. [In this section, we restrict attention to arm cavities with identical mirrors; in Appendix I we discuss generalizations to arm cavities bounded by *nonidentical* mirrors.] In Table IV we summarize the optimal (i.e. lowest value of  $I/I_{\text{BL}}$ ) configurations we found for each class. The results of items tabulated in this section are applied, in MBI Sec. III (cf. MBI Table I), to produce advanced LIGO designs with lower thermoelastic noise than the baseline design.

Our evaluations have been performed independently by all three co-authors (RO'S, SS, and SV), using multiple methods (both finite-element solutions and infinite-sum analytic solutions) when appropriate.

#### A. Baseline advanced LIGO configuration

The baseline design of an advanced LIGO interferometer [1] has four identical cylindrical sapphire test masses (i.e. physical radius  $R_p = 15.7$  cm; thickness  $H = 13$  cm; mass 40 kg) whose surfaces are coated over most of their surface (i.e. out to a radius  $R = R_p - 8$  mm). These mirrors' surfaces are designed so the largest possible Gaussian consistent with the 10 ppm diffraction loss constraint (Sec. II D) resonates in the arm cavity [i.e. a Gaussian beam with radius  $r_o = 4.23$  cm =  $1.63b$ ; cf. Appendix F and MBI Eq. (2.8)] for a discussion of Gaussian beams].

The thermoelastic noise integral for an arm cavity bounded by cylindrical mirrors and using a Gaussian beam is found by (i) constructing the Gaussian amplitude function  $u_G(r, r_o)$  [MBI Eq. (2.8)] and its associated beam intensity profile  $P(r) = |u_G(r, r_o)|^2$ ; (ii) solving for the elastic expansion  $\Theta$  that arises due to  $P(r)$  in the elastic model problem of Eq. (10) described in Sec. II B (cf. Sec. V A for numerical methods); and (iii) inserting the resulting expansion into the definition of the thermoelastic noise integral  $I$  [Eq. (9)]. For the baseline beam and test mass, the resulting value of the noise integral  $I$  is

$$I_{\text{BL}} = 2.57 \times 10^{-28} \text{s}^4 \text{g}^{-2} \text{cm}^{-1}. \quad (52)$$

[The advanced LIGO cylindrical mirrors and Gaussian beams are optimal: these beams produce very nearly the lowest thermoelastic noise possible using Gaussian beams reflecting off identical 40 kg cylindrical mirrors, where those cylinders are coated out to a radius  $R = R_p - 8$  mm

TABLE I: The thermoelastic integral  $I$  for a cylindrical test mass and a Gaussian beam, in units of the value  $I_{\text{BL}} = 2.57 \times 10^{-28} \text{s}^4 \text{g}^{-2} \text{cm}^{-1}$  for the advanced LIGO baseline design. The values of  $I/I_{\text{BL}}$  are estimated to be accurate to within one per cent.

$R$	$R_p$ [cm]	$H$ [cm]	$r_o$	$r_o/b$	$I/I_{\text{BL}}$	$\mathcal{L}_0$ [ppm] <sup>a</sup>	
BL <sup>b</sup>	$R_p - 8\text{mm}$	15.7	13.	4.23	1.63	1.000	10
	$R_p$	15.7	13.	4.49	1.73	0.856	10

<sup>a</sup>Diffraction losses in each bounce off the test mass, in ppm (parts per million), computed in the clipping approximation

<sup>b</sup>Baseline design for Advanced LIGO interferometers

and where the diffraction losses per bounce are restricted to less than 10 ppm.]

### B. Improved baseline advanced LIGO configuration

The conventional baseline described above wastes the last 8mm of mirror face size. We can improve upon the thermoelastic noise merely by eliminating the uncoated ring in the last 8mm, i.e. by coating the mirror out to the edge and adjusting the beamspot size to fill in the extra space. If the mirror coating extends out to the test-mass edge so  $R = R_p = 15.7$  cm, and the Gaussian beam radius is correspondingly increased to  $r_o = 4.49$  cm so the diffraction losses are still 10 ppm, then the thermoelastic noise is reduced to  $I/I_{\text{BL}} = 0.856$ ; see Table I.

[Again, the *same* advanced LIGO cylindrical mirrors (i.e. with unchanged physical radius and thickness) produce very nearly the lowest possible thermoelastic noise, among all 40 kg cylindrical mirrors coated out to their physical radius.]

### C. Mesa beams reflecting off identical 40kg cylindrical mirrors

Arm cavities with *mesa beams* reflecting off cylindrical mirrors admit configurations with even lower thermoelastic noise than the improved baseline. To explore the advantages of mesa beams, we evaluated the thermoelastic noise integral (via the method described in Sec. II E) for two one-parameter<sup>23</sup> families of cylindrical mirrors and mesa beams: 40 kg mirrors with the largest possible mesa beams resonating off their front faces (i.e. set by 10ppm diffraction losses; cf. Sec. II C 5),<sup>24</sup> coated ei-

<sup>23</sup> The arm cavity has three free parameters (mirror radius; mirror thickness; and mesa-beam radius parameter  $D$ ) and two constraints (mirror mass and diffraction losses per bounce).

<sup>24</sup> As expected, thermoelastic noise decreased with increasing mesa beam radius; we obtain the lowest value of thermoelastic noise integral  $I$  when the mesa beam radius is as large as possible, consistent with the diffraction constraint.

TABLE II: The thermoelastic integral  $I$  for a cylindrical test mass and a mesa beam, in units of the value  $I_{\text{BL}} = 2.57 \times 10^{-28} \text{s}^4 \text{g}^{-2} \text{cm}^{-1}$  for the Advanced LIGO baseline design. The values of  $I/I_{\text{BL}}$  are estimated to be accurate to within one per cent. The first four test masses, like the baseline, are mirror coated only out to  $R = R_p - 0.8\text{cm}$ ; the last five are coated all the way out to the test-mass edge,  $R = R_p$ .

$R$ [cm]	$R_p$ [cm]	$H$ [cm]	$D/b$	$I/I_{\text{BL}}$	$\mathcal{L}_0$ [ppm] <sup>a</sup>
$R_p - 8\text{mm}$	14.67	14.79	3.00	0.414	10
$R_p - 8\text{mm}$	15.70	13.00	3.43	0.364	10
$R_p - 8\text{mm}$	17.11	10.87	4.00	0.442	10
$R_p - 8\text{mm}$	19.58	8.30	5.00	1.000	10
$R_p$	13.94	16.38	3.00	0.373	10
$R_p$	15.70	13.00	3.73	0.290	10
$R_p$	16.37	11.88	4.00	0.313	10
$R_p$	18.85	8.96	5.00	0.628	10
$R_p$	21.36	6.98	6.00	1.69	10

<sup>a</sup>Diffraction losses in each bounce off the test mass, in ppm (parts per million), computed in the clipping approximation

ther out to (i) their physical radius  $R_p$  or (ii) only out to  $R_p - 8$  mm. Table II summarizes our results for each one-parameter family.

Whether the mirror is coated out to the full physical mirror radius or not, in both cases quadratic fits to  $I/I_{\text{BL}}(R_p)$  give minima rather near the baseline physical radii  $R_p = 15.7$  cm. Indeed, to within our accuracy of computation, the same mirror shape used as the baseline advanced LIGO design ( $R_p = 15.70\text{cm}$  and  $H = 13.00\text{cm}$ ) gives the optimal thermoelastic noise for mesa beams with 10 ppm diffraction loss. The beam radii  $D$  and thermoelastic noise  $I/I_{\text{BL}}$  for these near-optimal mexican-hat test masses are shown in Table IV below.

### D. Mesa beams reflecting off identical 40kg frustum mirrors

Roughly speaking, two mirrors with a larger front face radius permit a wider beam to resonate in the arm cavity and yield even lower thermoelastic noise. Therefore, we explore arm cavities bounded by frustum-shaped mirrors (cf. footnote 1), which expand the front face of the mirror at the expense of the back face.

More specifically, we considered arm cavities resonating with mesa beams of beam radius parameter  $D$  bounded by 40 kg test-mass mirrors whose front and back faces were as small as diffraction losses would permit (i.e. the front face produces precisely 10 ppm diffraction losses with arm-cavity mesa beam light of scale  $D$ ; the back face produces precisely one percent diffraction losses for the same mesa-beam input light; cf. Sec. II D).<sup>25</sup> These

<sup>25</sup> While in principle we could consider any combination of front

TABLE III: The thermoelastic integral  $I$  for a frustum input test mass (ITM) and a Mesa beam, in units of  $I_{\text{BL}} = 2.57 \times 10^{-28} \text{s}^4 \text{g}^{-2} \text{cm}^{-1}$ . The values of  $I/I_{\text{BL}}$  are estimated to be accurate to within one per cent.

$R^a$	$R_{p1}[\text{cm}]$	$R_{p2}[\text{cm}]$	$H[\text{cm}]$	$D/b$	$I/I_{\text{BL}}$	$\mathcal{L}_0[\text{ppm}]^b$
$R_p - 8\text{mm}$	14.67	10.57	19.81	3.00	0.355	$10 \ \& \ 10^4$
$R_p - 8\text{mm}$	15.70	11.56	17.00	3.43	0.253	$10 \ \& \ 10^4$
$R_p - 8\text{mm}$	17.11	12.88	14.06	4.00	0.207	$10 \ \& \ 10^4$
$R_p - 8\text{mm}$	17.45	13.22	13.45	4.13	0.208	$10 \ \& \ 10^4$
$R_p - 8\text{mm}$	19.58	15.27	10.43	5.00	0.285	$10 \ \& \ 10^4$
$R_p$	13.94	9.88	22.24	3.00	0.345	$10 \ \& \ 10^4$
$R_p$	15.70	11.56	17.00	3.73	0.198	$10 \ \& \ 10^4$
$R_p$	16.37	12.19	15.49	4.00	0.175	$10 \ \& \ 10^4$
$R_p$	17.29	13.04	13.75	4.39	0.162	$10 \ \& \ 10^4$
$R_p$	18.85	14.58	11.33	5.00	0.193	$10 \ \& \ 10^4$
$R_p$	21.36	17.00	8.62	6.00	0.398	$10 \ \& \ 10^4$

<sup>a</sup>Radius  $R$  of the mirror-coated portion of both the inner and the outer faces of the test mass, in units of its physical radius  $R_p$ .

<sup>b</sup>Diffraction losses in each bounce off the test mass, in ppm (parts per million); the first number is for the light inside the arm cavity, on face 1 of the test mass (radius  $R_1$ ); the second number is for the light impinging from the beam splitter onto face 2 of the test mass (radius  $R_2$ ).

TABLE IV: Optimized test-mass and light beam configurations, their thermoelastic noise compared to the baseline. [A subset of this table appears as Table I in MBI [4].]

Test Masses	Beam Shape	$\left(\frac{S_h}{S_{\text{BL}}}\right)_{\text{TE}}$
$\{R_{p1}, R_{p2}; H\}$		
BL: cylinders, $R = R_p - 8\text{mm}$ {15.7, 15.7; 13.0}	BL: Gaussian $r_o = 4.23\text{cm}$	1.000
BL: cylinders, $R = R_p - 8\text{mm}$ {15.7, 15.7; 13.0}	mesa $D/b = 3.73$	0.364
identical frustums, $R = R_p - 8\text{mm}$ {17.11, 12.88, 14.06}	mesa $D/b = 4.00$	0.207
BL: cylinders, $R = R_p$ {15.7, 15.7; 13.0}	Gaussian $r_o = 4.49\text{cm}$	0.856
BL: cylinders, $R = R_p$ {15.7, 15.7; 13.0}	mesa $D/b = 3.73$	0.290
identical frustums, $R = R_p$ {17.29, 13.04, 13.75}	mesa $D/b = 4.39$	0.162

arm cavities satisfy advanced LIGO design constraints (cf. Sec. IID).

Table III summarizes the thermoelastic integrals  $I/I_{\text{BL}}$  for two one-parameter family of designs: (i) the mirror is coated out to its physical radius  $R = R_p$  and (ii) the mirror is only coated out to  $R = R_p - 8\text{mm}$ . By fitting a

and back face radii  $R_1$  and  $R_2$  and any mesa beam radius  $D$  such that all three satisfy the LIGO design constraints presented in Sec. IID, we found that for  $R_2$  greater than or equal to the minimum radius allowed by diffraction losses the thermoelastic noise integral increases with  $R_2$  (for fixed mirror mass and front face size). Therefore, we limited attention to  $R_2$  as small as possible. Also, as usual, we limited attention to mesa beams as large as diffraction losses on the mirror front face permit.

quadratic to  $(D/b, I/I_{\text{BL}})$ , we estimate the optimal mirror dimensions and associated beam radii  $D$ . Our optimal results appear in Table IV.

## VII. INTERFEROMETER SENSITIVITY TO MIRROR PERTURBATIONS

In Sec. VI, we found mirror and beam configurations for the advanced LIGO arm cavity which indeed possess lower thermoelastic noise than the baseline advanced LIGO design. But our primary modification—the change to Mexican-hat optics for the cavity arms—involves employing mirrors which have never before been used in an interferometer. Naturally, then, we must make every effort to demonstrate that this radical proposal will not introduce new problems.

For example, the Mexican-hat mirror has a very flat central region (cf. Fig. 1). In our early presentations of this proposal, it was suggested to us that such a mirror design might make the resulting interferometer substantially more susceptible to errors, be they from static tilts and displacements or mirror figure error.

In this section, we examine this concern by examining the effect of perturbations on both gaussian and mesa-beam arm cavities. More explicitly, we by applying the tools described in Sec. IV to two fiducial beams (cf. MBI Sec. IV A 1):

- *Fiducial mesa beam and fiducial Mexican-hat mirrors*: The fiducial mesa-beam arm cavity, described in Sec. III A 1, which has mesa beams with  $D = 4b = 10.4 \text{ cm}$ .
- *Fiducial Gaussian beam and fiducial spherical mirrors*: A fiducial Gaussian beam arm cavity, which has beam radius  $r_o = 4.70 \text{ cm}$  (i.e. a  $g$ -value  $g = 0.952$ ).<sup>26</sup> [This fiducial Gaussian-beam arm cavity *differs* from the baseline (cf. MBI Sec. IV A 1).] The fiducial Gaussian beam cavity is chosen to have the same diffraction losses, on a mirror of the same coated radius, as the mesa-beam arm cavity (i.e. so the two fiducial cavities we compare are similar).

Using these two fiducial beams, we demonstrate that mesa-beam and Gaussian-beam interferometer designs for advanced LIGO will have broadly (i.e. within a factor  $\sim$  a few) similar sensitivity to perturbations. In short, we demonstrate that the mesa-beam proposal will not introduce undue sensitivity of the arm cavities and interferometers to mirror errors.

<sup>26</sup> The value  $g = 1 - L/\mathcal{R}_j$ , for  $\mathcal{R}_j$  the radius of curvature of spherical mirrors, can be related to the Gaussian beam radius  $r_o$  using formulae presented in Appendix F.

### A. Frequency distribution of parasitic modes as a measure of arm cavity sensitivity to perturbations

Given the denominators present in Eqs. (31) and (32), a system will generically be more unstable to perturbations if the eigenphases of excited modes [i.e.  $\arg(\eta_k)$ ] are close to the eigenphase of the resonant state. We can therefore crudely characterize the influence of generic perturbations by the distribution of eigenmodes nearby the ground state, also called the parasitic mode distribution. This discussion provides the basis for MBI Sec. IV B.

The resonant frequencies  $\omega = kc$  are determined when, after one round trip through the arm cavity, light in a given state interferes constructively with itself. Therefore, the light must be in an eigenstate  $|p\rangle$  of the cavity [Eq. (13)] and, moreover, the frequency of the light must be chosen so the eigenvalue of the round-trip eigenequation is *real*, or chosen so [cf. Eq. (14)]

$$2\pi n = 2L\omega/c + \text{Arg}(\eta_p) \quad (53)$$

for  $n$  some integer. The same eigenmode  $|p\rangle$  resonates at a specific frequency, and every other frequency separated from that frequency by the free spectral range  $\omega_{FSR} = \pi c/L$ . Within each free spectral range, different eigenmodes (i.e.  $|p\rangle, |q\rangle$ ) occur at different frequencies, separated by an amount uniquely determined by their eigenvalues  $\eta$ :

$$\Delta\omega_{pq} \equiv \omega_p - \omega_q = \frac{c}{2L} [\text{Arg}(\eta_p) - \text{Arg}(\eta_q)] . \quad (54)$$

For Gaussian beams, the eigenmodes are distributed within each free spectral range regularly; each nearest neighbor is separated by frequency [cf. Eq. (F4)]

$$\begin{aligned} \Delta\omega &= \frac{c}{L} \times \cos^{-1} g = \omega_{FSR} \times \frac{\cos^{-1} g}{\pi} \\ &= 0.099 \times \omega_{FSR} , \end{aligned} \quad (55)$$

using the  $g$ -value  $g = 0.952$  for our Gaussian baseline beams.

For the mesa beams, the frequency distribution of parasitic modes must be obtained numerically, by (i) solving the eigenequation for the eigenvalues  $\eta_p$  [Eq. (13), or equivalently Eq. (28), using the numerical methods of Sec. V B] and then by (ii) using those eigenvalues in Eq. (54) to deduce  $\Delta\omega_{p0}$  and therefore the distribution of parasitic modes. Table V lists the values for  $\Delta\omega_{p0}/\omega_{FSR}$  for a few states. Among states with low diffraction losses (i.e. with  $\mathcal{L} = 1 - |\eta_p|^2 < 10^{-2}$ ), most modes are very well separated from the ground state; the nearest parasitic mode of a mesa beam cavity is only a factor  $\sim 2.5$  closer to the ground state frequency than the nearest parasitic mode of a Gaussian-beam arm cavity. Therefore, as discussed in MBI Sec. IV C, we crudely expect the mesa-beam cavity to be only marginally more sensitive to perturbations than a Gaussian-beam arm cavity.

TABLE V: For a LIGO arm cavity with fiducial Mexican hat mirrors ( $D/b = 4$ ,  $R = 16$  cm), this table gives the separation  $\Delta\omega/\omega_{FSR}$  of the eigenfrequencies of parasitic modes from the eigenfrequency of the fundamental mesa-beam mode. [The table is indexed by two numbers,  $p$  and  $l$ , because the parasitic modes may be written in the form  $u(\vec{r}) = R_{p,l}(r) \exp(\pm il\theta)$ ; cf. Sec. V B. The index  $p$  is the number of radial nodes in the eigenfunction  $R_p(r)$ .]

	$l = 0$	$l = 1$	$l = 2$	$l = 3$
$p = 0$	0.0	0.0404	0.1068	0.1943
$p = 1$	0.1614	0.2816	0.4077	-0.4581
$p = 2$	0.4303	-0.4140	-0.2570 <sup>a</sup>	-0.0812 <sup>a</sup>
$p = 3$	-0.2330 <sup>a</sup>	-0.0488 <sup>a</sup>	0.1406 <sup>a</sup>	— <sup>a</sup>

<sup>a</sup>If the cavity length is adjusted so this mode is resonant, then its diffraction losses  $\mathcal{L}$  in each bounce off the test mass exceed 10000 ppm (i.e. one percent, in contrast with the fundamental mode's 18 ppm), so it cannot resonate strongly.

### B. Effect of displacement on cavities bounded by spherical and Mexican-hat mirrors

The discussion of the previous section gives us good reason to believe that mesa-beam and gaussian-beam arm cavities will display the same sensitivity (i.e. within a factor  $\sim 2.5$ ) to mirror perturbations. Here, we test this proposition when the ETM is displaced through a distance  $\vec{s} = s\hat{x}$  – or, more explicitly, when mirror 2 is perturbed by  $\delta h_2 = \delta h_{\text{disp}}$ , given by

$$\begin{aligned} \delta h_{\text{disp}} &= (\vec{s} \cdot \vec{r}) \frac{1}{r} \frac{dh_2}{dr} \\ &+ \frac{1}{2} \frac{|\vec{s} \times \vec{r}|^2}{r^3} \frac{dh_2}{dr} + \frac{1}{2} \frac{(\vec{s} \cdot \vec{r})^2}{r^2} \frac{d^2 h_2}{dr^2} \\ &+ O(s^3) \\ &= (xs) \frac{1}{r} \frac{dh_2}{dr} + \frac{1}{2} \frac{(xs)^2}{r^2} \frac{d^2 h_2}{dr^2} \\ &+ \frac{1}{2} \frac{(ys)^2}{r^3} \frac{dh_2}{dr} + O(s^3) . \end{aligned} \quad (56)$$

Section IV E summarizes the step-by-step process we follow to explore the influence of perturbations (here, displacement). However, because we expect—and our calculations below confirm—that whatever the precise mirror shapes, the properties of the interferometer will depend only weakly on displacement,<sup>27</sup> we do not complete all the steps that procedure includes (e.g., we do not compute the change in thermoelastic noise or cavity gain with displacement).

<sup>27</sup> The natural length parameter for the problem is  $b = \sqrt{\lambda L/2\pi} = 2.6$  cm, the diffraction length. When we perform perturbation theory, we find results which vary in powers of  $s/b$ . Since the LIGO control system will control displacements to much smaller than 1 cm, displacements have a relatively small effect on the LIGO interferometer.

### 1. Displacement of fiducial spherical mirrors

To evaluate the perturbation expansion [Eqs. (32) and (34)] for a cavity bounded by two identical fiducial spherical mirrors subjected to a displacement of its ETM through a distance  $s$  [Eq. (56)], we use analytic techniques specialized to spherical mirrors (e.g., Hermite-Gauss basis functions; cf. Appendix F). After some algebra (described in detail in Appendix F), we find the ground state of the perturbed cavity, to first order, to be [cf. MBI Eq. (4.12)]

$$|u\rangle = |0\rangle + \zeta_1^{\text{sph}} |1, 0\rangle + \mathcal{O}(s^2), \quad (57a)$$

$$\begin{aligned} \zeta_1^{\text{sph}} &= \frac{(1-g)^{1/4}}{\sqrt{2}(1+g)^{3/4}} (s/b) \\ &= 0.008(s/1 \text{ mm}). \end{aligned} \quad (57b)$$

[For clarity and for consistency with other work, we have absorbed a phase into the definition of the  $|1, 0\rangle$  Hermite-Gauss state.] Here,  $g \equiv 1 - L/R_c = 0.952$  is the  $g$ -value for the two fiducial spherical mirrors.

### 2. Displacement of fiducial Mexican-hat mirrors

Similarly, if we repeat the above calculation for Mexican-hat mirrors using the methods summarized in Sec. IV E, we find the ground state of the cavity changes to [cf. MBI Eq. (4.12)]

$$|\psi\rangle = |0\rangle + \zeta_1^{\text{MH}} |w_1\rangle + \mathcal{O}(d^2) \quad (58a)$$

$$|w_1\rangle \equiv |\psi^{(1)}\rangle / \zeta_1^{\text{MH}} \quad (58b)$$

$$\zeta_1^{\text{MH}} \equiv 0.263 (s/b) = 0.010 (s/1 \text{ mm}). \quad (58c)$$

Note that unlike the Gaussian-beam case,  $|w_1\rangle$  is a unit-norm *superposition* of eigenmodes of the unperturbed (mesa-beam) cavity, rather than an eigenmode of that cavity itself.

### 3. Power in parasitic modes

Perturbations cause changes in the resonant ground state. Equivalently, perturbations couple the ground state to the parasitic modes, causing power to leak from the resonant ground state of the unperturbed arm cavity into these other arm cavity eigenmodes.

In the case of displacement, the power in the parasitic modes is easily distinguished from the carrier light by symmetry: while the carrier light is axisymmetric, the lowest-order changes in state are dipolar (i.e.  $|\psi^{(1)}\rangle \propto |1, 0\rangle$  for Gaussian beams). The fraction of the total arm cavity light power in the *dipolar* parasitic modes is [cf. MBI Eq. (4.13)]

$$P_1 = \zeta_1^2 \simeq \begin{cases} 100(s/1.3\text{mm})^2 \text{ppm} & \text{sph,} \\ 100(s/1.0\text{mm})^2 \text{ppm} & \text{MH.} \end{cases} \quad (59)$$

[In deriving the above expression (59), we assume that for each displacement distance  $s$ , the input beam has been optimally tuned to match the arm cavity's perturbed ground state eigenfunction. In a sense, this expression measures the *intrinsic fraction* of power sent into parasitic modes by the applied perturbation (here, displacement of one ETM).

In practice, the arm cavity is driven by some fixed driving beam. As the mirror is displaced, the fraction  $|\gamma'_o(s)|^2$  of input laser power that enters the arm cavity will change [cf. Eq. (37)]. All this laser light enters the arm cavity's perturbed ground state. Of the power that enters the arm cavity, only a fraction  $\approx P_1$  enters parasitic modes. Therefore, relative to the total power beamed towards the arm cavity, only a fraction  $|\gamma'_o|^2 P_1$  enters parasitic modes.]

### 4. Power out the dark port

If one arm cavity's ETM is displaced, then the light leaving the two arm cavities will not interfere destructively at the dark port. The precise amount of power  $P_{\text{dp}}$  out the dark port depends on the driving beam [cf. Eq. (40), which depends on  $\gamma_0$ ,  $\gamma_1$ , and  $\gamma_2$ ]. If the interferometer is driven by the optimal Gaussian beam (cf. Sec. III A 2), then the power out the dark port is approximately entirely in a dipolar mode, with net power [i.e. Eq. (40) to lowest order, with  $\gamma_1 = 0$ ; cf. MBI Eq. (4.14)]

$$P_{\text{dp}}^{\text{total}} = \gamma_0^2 \zeta_1^2 \simeq \begin{cases} 90(s/1.3\text{mm})^2 \text{ppm} & \text{sph,} \\ 90(s/1.0\text{mm})^2 \text{ppm} & \text{MH.} \end{cases} \quad (60)$$

### C. Effect of tilt on the resonant eigenstate of an arm cavity bounded by spherical and Mexican-hat mirrors

Because both the spherical and Mexican-hat mirrors planned for advanced LIGO are very flat, the planned advanced LIGO arm cavities will necessarily be fairly sensitive to tilt.<sup>28</sup> This section demonstrates that, though Mexican-hat mirrors have a very flat central region—much more so than their spherical counterpart (cf. Fig. 2)—an arm cavity bounded by Mexican-hat mirrors will only be somewhat (i.e. a factor  $\sim$  few) more sensitive to tilt.

If the ETM of an arm cavity is tilted through an angle  $\theta_y$  about its  $y$  axis, the mirror surface is effectively

<sup>28</sup> For example, to order of magnitude, a tilt angle  $\theta \sim \sqrt{\lambda/2\pi L} = 6 \times 10^{-6}$  should produce a perturbation of order unity in the optical state of the cavity. Because an order-unity change in state implies fairly dramatic change in the interferometer, tilts much smaller still (of order few  $\times 10^{-8}$ ) can cause serious difficulty with the interferometer.

perturbed by  $\delta h_2 = \delta h_{\text{tilt}}$ :

$$\delta h_{\text{tilt}} = \theta_y x + O(\theta_y^3). \quad (61)$$

### 1. Tilt-induced changes in the arm cavity ground state

When this perturbation is inserted into the perturbation expansion (32) and the terms in that expansion are evaluated in the case of *spherical mirrors* (using special properties of spherical mirrors and Hermite-Gauss basis states; cf. Appendix F), we find first- and second-order corrections to the state [i.e terms in Eqs. (32) and (34)] to be given by [cf. MBI Eqs. (4.3) and (4.4)]

$$|\psi_1\rangle = \alpha_1^{\text{sph}} |(1, 0)\rangle, \quad (62a)$$

$$|\psi_2\rangle = \alpha_2^{\text{sph}} |(2, 0)\rangle, \quad (62b)$$

$$\begin{aligned} \alpha_1^{\text{sph}} &\equiv \frac{1}{\sqrt{2}(1-g^2)^{3/4}} (\theta_y \times \sqrt{kL}) \\ &= 0.0064(\theta_y/10^{-8}), \end{aligned} \quad (62c)$$

$$\begin{aligned} \alpha_2^{\text{sph}} &\equiv \frac{4}{\sqrt{2}(1-g^2)^{1/2}(1-g)} (\theta_y \times \sqrt{kL})^2 \\ &= 0.00046(\theta_y/10^{-8})^2. \end{aligned} \quad (62d)$$

Here  $g = 0.952$  is the  $g$ -value for the fiducial cavity, the states  $|(m, n)\rangle$  denote states in the Hermite-Gauss basis, and these states have been adjusted in phase to make  $\alpha_1$  and  $\alpha_2$  real.

If this same expansion is evaluated using *Mexican-hat mirrors* via the numerical procedure outlined in Sec. IV E, we find first- and second-order corrections to the state [i.e terms in Eq. (34)]. We will not provide an explicit form for these states here. These corrections have norms given by the Mexican-hat analogues of Eq. (62) for  $\alpha_1$  and  $\alpha_2$  [cf. MBI Eq. (4.5)]:

$$\begin{aligned} \alpha_1^{\text{MH}} &\equiv \|\psi^{(1)}\| = 14.78 (\theta_y \sqrt{kL}) \\ &= 0.0227(\theta/10^{-8}) \end{aligned} \quad (63a)$$

$$\begin{aligned} \alpha_2^{\text{MH}} &\equiv \|\psi^{(2)}\| = 74.97 (\theta_y \sqrt{kL})^2 \\ &= 0.00018(\theta_y/10^{-8})^2. \end{aligned} \quad (63b)$$

We can use these expressions to define normalized representations of the first- and second-order corrections:

$$u_1 \equiv \left| \psi^{(1)} \right\rangle / \alpha_1^{\text{MH}}, \quad (63c)$$

$$u_2 \equiv \left| \psi^{(2)} \right\rangle / \alpha_2^{\text{MH}}. \quad (63d)$$

We display contour maps of these normalized admixtures of modes in Fig. 5 of MBI [4].

### 2. Parasitic mode power excited by tilt

The largest correction to the perturbed arm cavity ground state is a *dipolar* perturbation (i.e.  $|(1, 0)\rangle$  for

Gaussians;  $|u_1\rangle$  for mesa beams). Therefore, interpreting this change as an excitation of dipolar parasitic modes, the fractional power in the dipolar parasitic modes is [cf. MBI Eq. (4.6)]

$$P_1 = \alpha_1^2 \simeq \begin{cases} 0.0005(\theta_y/3.5 \times 10^{-8})^2 & \text{sph,} \\ 0.0005(\theta_y/1.0 \times 10^{-8})^2 & \text{MH,} \end{cases} \quad (64)$$

when the ETM is tilted through an angle  $\theta_y$ .

### 3. Tilt-induced changes in the diffraction losses of the ground state of the resonant arm cavity (Mexican-hat only)

The diffraction losses associated with the ground state—which we approximate by the clipping approximation losses  $\mathcal{L}_1$  and  $\mathcal{L}_2$  [Eq. (16)]—also change when the beam state changes. As described in Sec. IV C 1, we find the perturbed value for, say,  $\mathcal{L}_1$  merely by expanding the expression for  $\mathcal{L}_1$ , obtaining the general expansion Eq. (36).

If we evaluate Eq. (36) for the case of a cavity bounded by two Mexican hat mirrors with one mirror (the ETM, i.e. mirror 2) tilted through an angle  $\theta_y$ , we find we can rewrite Eq. (36) for the losses at mirror 1 (the ITM) in terms of the expansion mentioned above (i.e. in terms of  $\alpha_1$ ,  $\alpha_2$ ,  $u_1$ , and  $u_2$ ):

$$\begin{aligned} \mathcal{L}'_1 &= \mathcal{L}_1 + \alpha_1^2 (\mathcal{L}_A^{(2)} - \mathcal{L}_1) + \alpha_2 \mathcal{L}_B^{(2)} \\ &\approx 18 \text{ ppm} [1 + 0.0025(\theta_y/10^{-8})^2] \end{aligned} \quad (65)$$

[cf. MBI Eq. (4.7)] where

$$\begin{aligned} \mathcal{L}_1 &= \langle u_o | O_1 | u_o \rangle = 18 \text{ ppm}, \\ \mathcal{L}_A^{(2)} &= \langle u_1 | O_1 | u_1 \rangle = 96 \text{ ppm}, \\ \mathcal{L}_B^{(2)} &= 2\text{Re} \langle u_o | O_1 | u_2 \rangle = 29 \text{ ppm}. \end{aligned} \quad (66)$$

and where  $u_1$  and  $u_2$  are defined by Eq. (63).

Using a similar technique we can also evaluate the change in the clipping approximation diffraction losses at mirror 2. [As discussed Sec. IV D 2, we for simplicity assume the diffraction losses at both mirrors remained the same as the mirror tilted, or  $\mathcal{L}_1 = \mathcal{L}_2$ . Since the diffraction losses influence physical quantities like the cavity gain fairly little, we require only a rough estimate of their sensitivity to perturbations.]

## D. Effect of tilt on arm cavities and interferometers using Mexican-hat mirrors but driven by Gaussian beams

Tilt of one ETM causes changes in several important properties of an interferometer that uses mesa beams (and is driven by the optimal Gaussian): (i) the amount of thermoelastic noise present in the dark port signal; (ii) the amount of power present in the perturbed arm



cavity (i.e. the arm cavity gain); and (iii) the amount of input light power leaving the dark port. In this section we compute the changes in these three quantities by applying the general techniques presented in Sec. IV C to the case of tilt.

### 1. Tilt and thermoelastic noise

To lowest order in  $\theta_y/(b/L)$ , tilt has *no effect* on thermoelastic noise: at first-order, tilt only excites odd-parity modes, which produce nonaxisymmetric intensity perturbations, and nonaxisymmetric intensity perturbations do not contribute to lowest-order changes in the thermoelastic noise integral (cf. Sections IV C 4 and IV D 1).

### 2. Tilt and cavity gain, when driven by a Gaussian beam

Equation (38) provides a general expression for the cavity gain for a perturbed cavity; this expression depends on (i) the amount of light power  $\gamma'_o$  entering the perturbed arm cavity [Eq. (37), evaluated using the perturbed mesa-beam state from Eq. (63)], which we can express using the perturbation parameters  $\gamma_1$  and  $\gamma_2$ ,

$$\gamma_1 = 0 \quad \gamma_2 = -0.070 + 0.013i; \quad (67)$$

and (ii) on the diffraction losses of the resonant state of the tilted arm cavity [Eq. (65) above].<sup>29</sup> Combining these expressions, we find the arm cavity power, relative to the input beam power, to be given by [cf. MBI Eq. (4.8)]

$$\begin{aligned} \mathcal{G}'_{\text{anal}} &= \mathcal{G}_{\text{anal}} \left[ 1 - \alpha_1^2 + \frac{\alpha_2}{\gamma_0} (\gamma_2 + \gamma_2^*) - 2 \frac{\mathcal{L}'_1 - \mathcal{L}_1}{1 - r_I} \right] \\ &= 737 \left[ 1 - 5.5 \times 10^{-4} (\theta_y/10^{-8})^2 \right]. \end{aligned} \quad (68)$$

### 3. Tilt and dark port power, when driven by a Gaussian beam

Finally, when one ETM mirror in a mesa-beam interferometer is tilted, the beamsplitter sends light to the dark port. Equation (40) provides a general expression for the light  $u_{\text{dp}}$  leaving the interferometer through the dark port; for tilt, this expression evaluates to

$$u_{\text{dp}} = \sqrt{2} \left[ (-\gamma_o \alpha_1^2 + \gamma_2 \alpha_2) |u_o\rangle + \alpha_1 \gamma_o |u_1\rangle + \alpha_2 \gamma_o |u_2\rangle \right] \quad (69)$$

where we use (i) the definitions  $\alpha_1 = \|\psi^{(1)}\|$  and similarly [cf. Eq. (63)], and (ii)  $\gamma_1 = 0$ , to simplify the general equation (40).

The corresponding fraction of the interferometer's power that exits the interferometer through the dark port in the fundamental mode  $u_o$  and in the parasitic modes  $u_1$  and  $u_2$  is [cf. MBI Eq. (4.9)]; note the MBI expression will be larger by a factor 4!<sup>30</sup>

$$P_{\text{dp},0} = |-\gamma_o \alpha_1^2 + \gamma_2 \alpha_2|^2 \simeq 0.256 (\theta_y/10^{-8})^4 \text{ ppm} \quad (70a)$$

$$P_{\text{dp},1} = \gamma_0^2 (\alpha_1^{\text{MH}})^2 \simeq 478 (\theta_y/10^{-8})^2 \text{ ppm}, \quad (70b)$$

$$P_{\text{dp},2} = \gamma_0^2 (\alpha_2^{\text{MH}})^2 \simeq 0.024 (\theta_y/10^{-8})^4 \text{ ppm}. \quad (70c)$$

## E. Effect of mirror figure error on mesa-beam interferometers

In this section, we explore the sensitivity of individual arm cavities and the overall interferometer to mirror figure error, when the beam resonating in the arm cavities is a fiducial mesa beam. More specifically, in this section we (i) distort the ETM by a physically plausible amount (i.e. an amount estimated from actual mirror figure error measurements of LIGO mirrors); (ii) apply perturbation theory (cf. Sec. IV E) to deduce the change in resonant ground state of the arm cavities; and then (iii) use the resulting modified beam state to deduce how the power spectrum of thermoelastic noise will change due to the perturbed beam cross section.

MBI [4] uses the computations performed in this section to place constraints on the accuracy of machining required of the mirrors used in a mesa-beam interferometer; cf. MBI Sections IV F and IV G.

### 1. GLB's worst-case figure error

GariLynn Billingsley has provided us with a map of a worst-case figure error,  $\delta z_{\text{wc}}(x, y)$  [height error as function of Cartesian coordinates in the transverse plane], produced by current technologies. Her map is based on the measured deviation of a LIGO-I beam-splitter substrate from flatness. The measured substrate had diameter 25 cm; she stretched its deviation from flatness (its “figure map”) to the baseline advanced LIGO mirror diameter of 35.4 cm, fit Zernike polynomials to the stretched map, and smoothed the map by keeping only the lowest 36 Zernikes. MBI Fig. 6 provides a contour diagram of the resulting figure map (figure “error”). In the central region (innermost 10 cm in radius), the peak to valley error  $\Delta z$  is about 30 nm, while in the outer region (10 cm to 16 cm in radius), it is about 110 nm.

Billingsley (private communications) thinks it likely that in the central region (which dominates our considerations), peak-to-valley errors of  $\Delta z \sim 5$  nm (about 1/5

<sup>29</sup> When computing the diffraction losses for a tilted cavity, we assume the same diffraction losses associated with a bounce off mirror 1 and mirror 2.

<sup>30</sup> The MBI expression estimates the effect when all four mirrors are tilted about uncorrelated axes; it therefore is larger than our result, which describes the effect of tilting only one mirror.

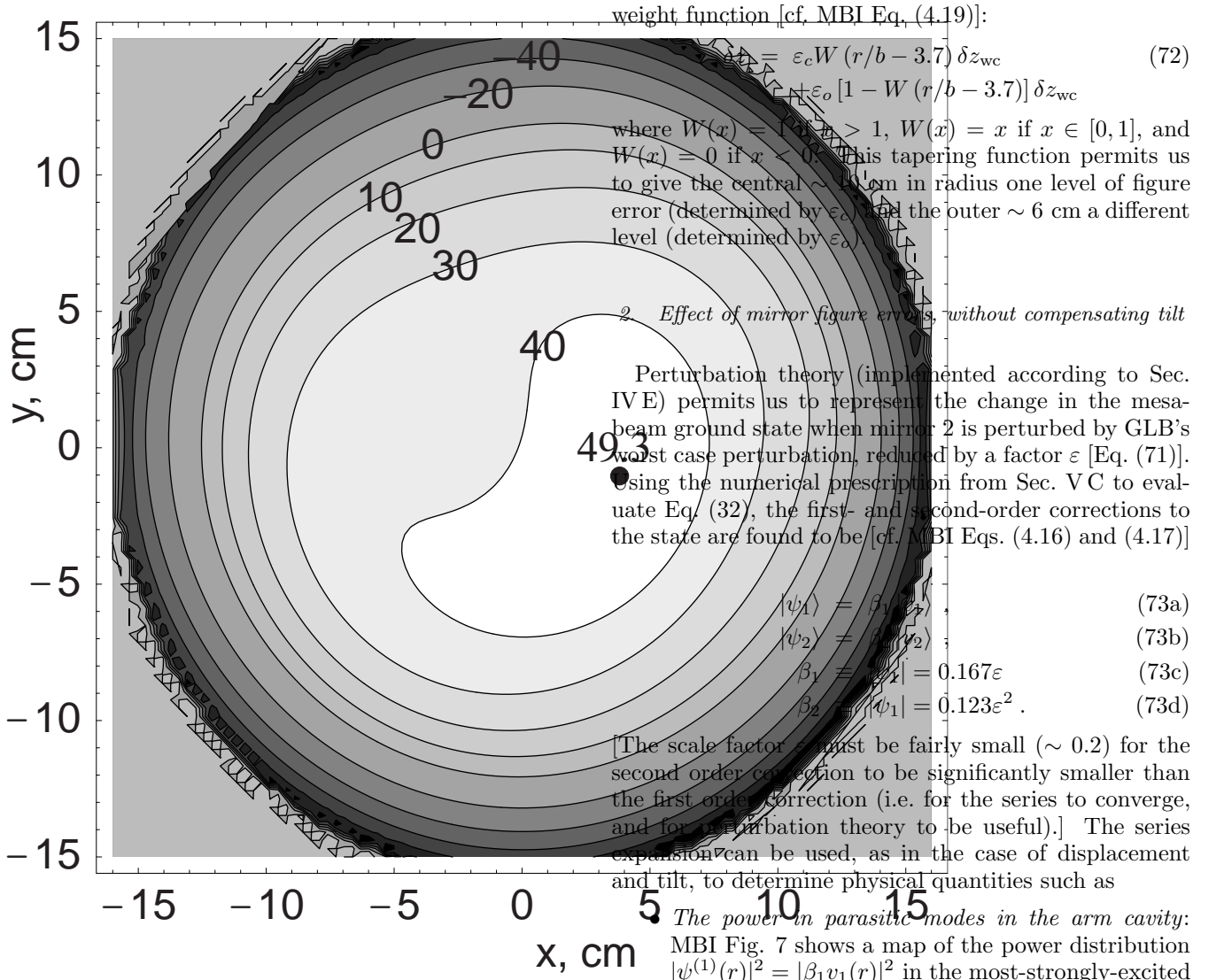


FIG. 5: Contour diagram of GariLynn Billingsley's worst-case mirror figure error [height  $\delta z_{wc}$ ] in nanometers, cf. MBI Fig. 6.

as large as in MBI Fig. 6) may be achievable; Jean Marie Mackowski believes even smaller errors can be obtained with coating methods (cf. MBI Sec. IV F 1). Accordingly, in the analyses described below we shall use Billingsley's map, scaled down in height by a factor  $\varepsilon$  [cf. MBI Eq. (4.15)]:

$$\delta z = \varepsilon \delta z_{wc}(x, y), \quad (71)$$

and we shall use  $\varepsilon = 0.2$  and  $\Delta z = 6$  nm as our fiducial values for  $\varepsilon$  and  $\Delta z$ .

Also, Billingsley thinks it likely that the outer regions of the mirror will be of significantly lesser quality than the inner regions. To study the sensitivity of the interferometer and thermoelastic noise to errors in the exterior, we divided GLB's perturbations into two regions by a

<sup>31</sup> Unlike displacement and tilt, for mirror figure error  $\gamma_1$  is generically nonzero, since the perturbation admits an axisymmetric part.

Naturally, the interferometer is more sensitive to errors in the inner  $\sim 10$  cm, where the beam power is large, than to the outer  $\sim 6$  cm, where the beam power is small. To investigate this effect, we considered height perturbations of the form discussed in Eq. (72); to characterize the sensitivity of the beam shape to these defects, we examined the norm  $\beta_1^2 = \|\psi^{(1)}\|^2$  [Eq. (73)], which is necessarily a quadratic form in  $\varepsilon_c$  and  $\varepsilon_o$  [cf. MBI Eq. (4.20)]. Using the same methods as for Eq. (73), we found the norm  $\beta_1^2$  to be

$$\begin{aligned} \beta_1^2 &= 0.028\varepsilon_c^2 + 1.06 \times 10^{-3}\varepsilon_o(\varepsilon_o - \varepsilon_c) \\ &\approx 0.0011(\varepsilon_c/0.2)^2 + 4.3 \times 10^{-5}(\varepsilon_o/0.2)(\varepsilon_o - \varepsilon_c)/0.2. \end{aligned} \quad (76)$$

If  $\beta_1$  is used as a characteristic example of the sensitivity of physical quantities (e.g., the power out the dark port) to height perturbations, then a mesa-beam interferometer is around 5 times more sensitive to mirror figure errors in the interior region of each test-mass mirror (i.e. its inner  $\sim 10$  cm) than it is to perturbations outside that region.<sup>32</sup>

### 3. Mirror figure errors, with compensating tilt

The tilt control system automatically and dynamically reorients the mirrors in response to what it interprets as tilt. Specifically, the mirror tilt control system (i) *measures signals containing information about beam asymmetry*, such as the output of a quadrant photodiode; (ii) *computes the mirror tilt that would generate these asymmetries* using perturbation theory expansions [i.e. Eq. (32), to first order]; and then (iii) *tilts all four LIGO mirrors to eliminate the apparent tilts* that the system computed in the previous step. Therefore, since mirror figure error *also* produces beam asymmetries, the tilt control system of the interferometer will act to partially compensate (the dipolar part of) the static mirror defect.

The precise quantity the tilt control system measures to deduce the tilt angle is not important: different approaches to tilt control interpret the optical state of our arm cavity [i.e. interpret the state  $|u'_o\rangle$  defined by the corrections in Eq. (73)] in a manner fairly independent of the method used (i.e. the compensating tilt we calculate depends little on the method we use to calculate it).

<sup>32</sup> In our perturbative computations, the mirrors were treated as *infinite*. The infinite-mirror model proves sufficiently accurate for perturbations in the center 10cm of the mirror. Unfortunately, for mirror defects in the outer 6cm, the resulting perturbed state has diffraction losses roughly comparable to the effect of the perturbation. Therefore, our perturbative simulations of mirror defects in the outer  $\sim 6$ cm in general, and the coefficients of  $\varepsilon_o$  in Eq. (73) in particular, are not reliable. By contrast, in her simulations Erika D'Ambrosio used realistic finite mirrors [6]. As discussed in MBI [cf. MBI Eq. (4.20)], she finds the inner region to be about 3.5 times more sensitive to mirror perturbations than the outer region.

In this section, we assume the tilt control system acts to minimize the dipolar component of the arm cavity beam power.

Therefore, we find the tilt-compensated state by (i) adding together the results of a tilt perturbation [i.e. a generalization of Eq. (62) that depends on two tilt angles,  $\theta_x$  and  $\theta_y$ ] and the mirror figure error perturbation [Eq. (73), which depends on  $\varepsilon$ ]; (ii) evaluating the norm  $\|\psi^{(1)}\|$  of the first-order perturbation; and then (iii) finding the tilt angles  $\theta_x$  and  $\theta_y$  which minimize that norm. The resulting optimal tilt angle is [cf. MBI Sec. IV H 3]

$$\theta_x = +0.98 \times 10^{-8}(\varepsilon/0.2), \quad (77a)$$

$$\theta_y = +0.69 \times 10^{-8}(\varepsilon/0.2), \quad (77b)$$

$$\theta = \sqrt{\theta_x^2 + \theta_y^2} = 1.2 \times 10^{-8}(\varepsilon/0.2) \quad (77c)$$

(in the limit of small  $\varepsilon$ , so linear theory applies). MBI Figure 8 shows the height of the surface of the mirror after the compensating tilt is applied.

After the tilt is applied, the first-order correction to the resonant mesa-beam state is a combination of tilt and mirror-figure perturbations. For brevity, we denote the net first-order correction to the mesa-beam state when tilt is applied by

$$|\psi^{(1)}\rangle = \beta_{1,c} |v_{1,c}\rangle, \quad (78a)$$

$$\beta_{1,c} \equiv \|\psi^{(1)}\| 0.02(\varepsilon/0.2). \quad (78b)$$

The square of the norm (i.e.,  $\beta_{1,c}^2$ ), as usual, is the fraction of arm cavity power which is in parasitic modes [cf. MBI (4.23)]:

$$P_{1c}^{\text{arm}} = |\beta_{1,c}|^2 = 0.0004(\varepsilon/0.2)^2. \quad (79)$$

MBI Figure 9 shows a map of the power in parasitic modes,  $|\beta_{1,c} v_{1,c}(r)|^2$ . Also, the norm of this first-order correction provides an estimate of the power leaving the dark port of this interferometer (i.e. an interferometer with one tilted, defective mirror) when the interferometer is driven with Gaussian beams [i.e. Eq. (40) to lowest order; cf. MBI (4.24)]:<sup>33</sup>

$$\begin{aligned} P_{dp} &\approx (|\gamma_o|^2 + |\gamma_1|^2) |\beta_{1,c}|^2 \\ &\simeq \gamma_o^2 |\beta_1|^2 = 0.00038(\varepsilon/0.2)^2 \end{aligned} \quad (80)$$

### 4. Influence of mirror figure errors on thermoelastic noise

Because the ETM's figure error distorts the beam resonating in the arm cavity, the thermoelastic noise produced by each mirror bounding that arm cavity changes by some small amount. Given the change in state deduced above, we know how the beam profile at the ITM

<sup>33</sup> As in the untilted case, we neglect the (nonzero) term  $|\gamma_1|^2$ .

changes. We can therefore evaluate, using the discussion of Sec. IV C, the change in thermoelastic noise associated with the beam reflecting off the ITM's face.

To be explicit, to compute the first-order effects of a perturbation  $\delta P$  to the thermoelastic noise integral  $I_1$  of mirror 1 in this fiducial case, we first select the axisymmetric portion  $\delta P_o(r) = \int d\varphi P(\vec{r})/2\pi$  of  $\delta P$ ; we then linearize the analytic expressions derived by Liu and Thorne for cylindrical mirrors (cf. Sec. V A 2), using  $\delta P_o$  as the magnitude of the perturbation<sup>34</sup>; and finally we extract from this linearization the first-order change in  $I_1$ .

When we apply this technique to the fiducial beam reflecting off a cylindrical mirror of radius 16 cm and thickness 13 cm which is deformed by GariLynn Billingsley's mirror distortion [Eq. (71)], we find the thermoelastic noise integral for that mirror changes to

$$I_1/(2 \times 10^{-28}) = 0.632 [1 + 0.035(\varepsilon/0.2)] \quad (81)$$

where  $I_1$  denotes the total thermoelastic noise integral for mirror 1 when mirror 2 is deformed by our scaled height perturbation (71). [Roughly speaking, we expect the beam and hence the thermoelastic noise to change in a qualitatively similar fashion at mirror 2 (cf. Sec. IV D 2)].

MBI Section IV G applies this result to deduce how sensitive the power spectrum of thermoelastic noise is to uncorrelated mirror figure errors on all four mirrors [cf. MBI Eq. (4.27)].

## VIII. CONCLUSIONS

In this paper, we have described both the theory and practice needed to obtain the results summarized in MBI. Specifically, we have developed analytic and numerical tools to evaluate the following:

- *Thermoelastic noise integrals*: We developed practical techniques for finding the thermoelastic noise for nonstandard optical systems (i.e. noncylindrical finite mirrors and unusual beam shapes) [Sections II B and V A]. We tabulated the thermoelastic noise, relative to the current advanced LIGO baseline, for many alternative mirror and beam configurations [Tables I - IV in Section VI]. We found many configurations with lower thermoelastic noise than the baseline advanced LIGO configuration.
- *Eigenmodes of an arm cavity bounded by Mexican-hat mirrors*: We also wrote numerical code to find the eigenmodes of an optical cavity [Sections II C and V B]. We computed and tabulated many of the

eigenmodes of an arm cavity bounded by Mexican-hat mirrors (none of which appear explicitly in this paper).

- *Second-order optical perturbation theory*: Finally, we developed expressions for second-order optical perturbation theory [Sec. IV]. We applied perturbation theory extensively to study the sensitivity of mesa-beam interferometers to perturbations (i.e. to mirror figure error, mirror tilt, and mirror displacement).

The results found here are used in MBI to conclude that mesa-beams interferometer designs offer clear advantages over the baseline advanced LIGO design, without being substantially more sensitive to mirror figure error, tilt, or displacement perturbations.

In MBI [4], in Erika D'Ambrosio's paper [6], and this paper, we and our collaborators have only taken the first steps towards the design of a practical mesa-beam advanced LIGO proposal. For example, more perturbative calculations—this time, applied to the final design, rather than to a fiducial case—are needed, for the design of the control system (i.e. so the relationship between light on various photodiodes and the correcting tilt applied to the LIGO mirrors can be established). Further, in this paper we have only begun to explore the space of all possible mirrors. For simplicity, we chose to fix the mirror mass to 40 kg. In practice, however, with sapphire, mirror designs are limited by fabrication limits (i.e. the radius of the mirror is limited by the radius of the sapphire boule one can grow) rather than by weight limits. Therefore, before a final design is chosen, more mirror designs (including cylinders with  $m > 40$  kg) should be examined. Finally, in this paper, our Mexican-hat designs were limited to symmetric cavities (i.e. using *identical* mirrors). In practice, asymmetric designs offer the possibility of lower thermoelastic noise and greater practical convenience<sup>35</sup>. Further work is necessary on the design, construction, and operation of asymmetric cavities with mexican-hat-like mirrors.

## Acknowledgments

Without the assistance of our collaborators on our extended project to study LIGO thermoelastic noise in the presence of Mexican-hat mirrors (Erika D'Ambrosio and Kip Thorne), this paper would never have appeared; we thank them for their support and their assistance with the text. We thank GaryLynn Billingsley for providing and explaining plausible deformations for LIGO mirrors.

<sup>34</sup> When linearizing the LT equations, the natural relationship between  $\delta P$  and  $\delta p_m$  follows from Eq. (43). Note, however, that  $p_o$  is independent of  $P(r)$  [because  $P(r)$  are all normalized] and thus  $\delta p_o = 0$ .

<sup>35</sup> For example, rather than design all four mirrors to be identical MH, one may want to operate with some spherical mirrors first, then replace a few mirrors (i.e. the ETMs) with MH-like mirrors later. Bill Kells has proposed using a flat ITM and first a spherical and then an MH-like ETM.

ROS thanks: Bob Spero for helpful discussion about practical computations of diffraction loss; Erika D’Ambrosio, for invaluable discussions on perturbation theory for optics, on assistance with references, and for helpful suggestions regarding thermoelastic noise simulations (i.e. on the choice of the set  $\mathcal{R}$ ); and Lee Lindblom, for helpful suggestions on the postprocessing numerical methods. He also thanks Guido Muller (our kind LSC reviewer) and Pavlin Savov for locating typographical errors in early drafts. ROS has been supported in part by NSF Grant PHY-0099568.

SS and SV thank: Vladimir Braginsky and Farid Khalili for stimulating discussion. This research was supported by NSF grant PHY-0098715, the Russian Foundation for Fundamental Research, Russian Ministry of Industry and Science, and (for SPV) by the NSF through Caltech’s Institute for Quantum Information.

## APPENDIX A: SAPPHIRE MATERIAL PARAMETERS: NOTATION AND VALUES

While sapphire is not an isotropic material, it can be reasonably approximated by isotropic elastic and thermodynamic properties. In this paper, we therefore treat sapphire as an isotropic medium, with the following specific values for physical parameters:<sup>36</sup>

$$E = 4 \times 10^{12} \text{erg/cm}^3 \quad (\text{A1})$$

$$\rho = 4.0 \text{ g/cm}^3 \quad (\text{A2})$$

$$\sigma = 0.28 \quad (\text{A3})$$

$$\alpha = 5.5 \times 10^{-6} \text{ K}^{-1} \quad (\text{A4})$$

$$\kappa = 3.3 \times 10^6 \text{ erg cm}^{-1} \text{ K}^{-1} \text{ s}^{-1} \quad (\text{A5})$$

$$C_V = 7.7 \times 10^6 \text{ erg g}^{-1} \text{ K}^{-1} \quad (\text{A6})$$

## APPENDIX B: GENERAL DESCRIPTION OF MESA BEAMS

In Section IIA we only briefly describe the form of mesa beams evaluated at the surfaces of an arm cavity’s two mirrors. In this appendix, we provide a much more thorough treatment of mesa beams.

### 1. Constructing mesa beams

Mesa beams are constructed by averaging some gaussian beams (with waist size  $A_o$  and waist location  $z_w$ ) over some disc of size  $D$  and then normalizing the result.

Specifically, we construct mesa beams that propagate towards positive  $z$  by first averaging a (non-normalized) gaussian beam over a disc of radius  $D$ :

$$U(\vec{r}, z, D) = e^{ikz} \times \int_{r' < D} d^2 r' U_g(\vec{r} - \vec{r}', z; \bar{z}, z_w) \quad (\text{B1a})$$

$$U_g(\vec{r}, z; \bar{z}, z_w) = \exp \left[ -\frac{r^2 \left[ 1 - i \frac{(z - z_w)}{\bar{z}} \right]}{2A_o \sqrt{1 + \frac{(z - z_w)^2}{\bar{z}^2}}} \right] \times e^{-i \tan^{-1}(z/\bar{z})} \quad (\text{B1b})$$

[where  $A_o$  is a function of  $\bar{z}$ , given by  $\bar{z} \equiv kA_o^2$ , and where  $z_w$  is the location of the beam waist]. The result of the average is necessarily axisymmetric. Since  $U(\vec{r}, z, D)$  is axisymmetric (because of the symmetric integral which defines it), we may normalize the result with a one-dimensional integral:

$$N^2(D, z) \equiv \int_0^\infty |U(r, z, D)|^2 2\pi r dr \quad (\text{B1c})$$

$$u_{\text{mesa}}(\vec{r}, z, D) \equiv U(r, z, D)/N(D, z) e^{ikz} \quad (\text{B1d})$$

To construct the associated Mexican-hat mirror which will reflect this mesa beam back into itself (propagating in the opposite direction) at location  $z_r$ , we require the Mexican-hat mirror height function  $h_{\text{MH}}$  to be continuous and to satisfy

$$u_{\text{mesa}}(r, z_r, D) \exp(-2ikh_{\text{MH}}) = u_{\text{mesa}}(r, z_r, D)^* \quad (\text{B2})$$

for  $u(\vec{r}, z_r, D)$  the values of a mesa beam at the mirror plane  $z = z_r$ . This expression is equivalent to MBI Eq. (2.13) [cf. Eq. (6) in this paper]. These requirement uniquely specify the Mexican-hat mirror shape  $h_{\text{MH}}$ .

#### a. Canonical mesa beams: mesa beams for symmetric cavities

The mesa beams presented in MBI and discussed henceforth in this paper — denoted *canonical mesa beams* — are assumed to have particularly special form. First, it is assumed that the cavity confining the mesa beam is symmetric, with mirror 1 placed at  $z = -L/2$  and mirror 2 placed at  $z = L/2$ ; also it is assumed that the waist location,  $z_w$ , is placed precisely between them (i.e  $z_w = 0$ ). Second, it is assumed that the gaussian used to construct the mesa beam is the *minimal-diffraction* gaussian for the symmetric cavity. The minimal diffraction gaussian has  $\bar{z} = L/2$  and  $z_w = 0$ , implying that the beam width is  $b = \sqrt{L/k}$  at the mirror surfaces and  $b/\sqrt{2}$  at the beam waist at  $z = 0$ .

#### 2. Canonical mesa beams at the mirror surfaces

In this paper and in MBI, we only need to know the form of canonical mesa beams at the mirror surfaces. In

<sup>36</sup> These numbers are taken directly from the advanced LIGO project book [1], and the advanced LIGO summary web page [3].

this case, since the beam is canonical (i.e. has symmetric cavities and minimal diffraction gaussians, so  $z_w = 0$  and  $\bar{z} = L/2$ , implying  $A_o = b/\sqrt{2}$ ) and since we evaluate it at the mirror surfaces  $z = \mp L/2$ , we find that Eq.(B1b) simplifies to

$$U_{g,\min}(\vec{r}, z = \mp L/2) = \exp\left[-\frac{r^2 [1 \pm i]}{2b^2}\right] e^{\pm i\pi/4} \quad (\text{B3})$$

Inserting this expression into the definition (B1) of general mesa beams, we find that the mesa beam form at mirror 1 (i.e. the mirror at  $z = -L/2$ ) is given in terms of the construction described in Eq. (5). [For simplicity, in Eq. (5) we omit the overall phase factor  $\exp(i\pi/4)$ .]

### APPENDIX C: CONVERTING THE FLUCTUATION-DISSIPATION MODEL PROBLEM TO A STATIC MODEL PROBLEM AT LOW FREQUENCIES

In Sec. II B, we claim that at low frequencies, the elastic response of a cylinder to an oscillating pressure profile can be reconstructed to a good approximation using the static response of a cylinder to the same pressure profile, in an appropriate accelerating frame.

Briefly speaking, a relationship between the dynamic and static problems exists because, when the oscillations are sufficiently slow, the effect of dynamical terms in the elastic equations of motions can be neglected. These physical considerations have been discussed at greater length elsewhere, cf. Sec. II of LT [12].

In this appendix, we demonstrate in more technical detail precisely how to establish the desired (approximate) relationship. We assume only basic familiarity with elasticity, on the level of Blandford and Thorne [14].

#### 1. General quasistatic approach for the elastic response to an oscillating surface stress

We wish to solve the elasticity equations, which can be expressed as

$$\rho \partial_t^2 y_a + \nabla^b T_{ab} = 0, \quad (\text{C1})$$

for a test-mass mirror subject to an oscillating surface stress on its inner face (i.e. on the surface  $z = 0$ , where the optic axis of the advanced LIGO arm cavity is the  $z$  axis),

$$T_{az}(t, r, z = 0) \equiv \bar{T}_{az}(r, z = 0) \cos(\omega t), \quad (\text{C2})$$

and otherwise subject to no other stresses. [Here,  $T_{ab}$  is given in terms of  $y_a$  by Eq. (10b).]

##### a. Step 1: Express the problem in the accelerated frame

We can better understand the response of the mirror substrate if we go into a frame comoving with the center

of mass of the test mass mirror. The test mass experiences a net force  $F_a \cos(\omega t)$ , determined by the surface stress:

$$F_a \equiv -\cos(\omega t) \int d^2 r \bar{T}_{az}(\vec{r}, z = 0). \quad (\text{C3})$$

In response to this net force, the mirror center of mass  $R_{\text{cm}}$  accelerates:

$$\ddot{R}_{\text{cm}} = -\frac{F_a}{M\omega^2} \cos(\omega t). \quad (\text{C4})$$

Therefore, to go to the comoving frame, we perform the following transformation: (i) define the comoving displacement field  $y'_a = y_a - R_{\text{cm}}$ :

$$y'_a \equiv y_a + \frac{F_a}{M\omega^2} \cos(\omega t); \quad (\text{C5})$$

(ii) define the comoving stress-energy tensor as  $T'_{ab} = T_{ab}(y')$ . In terms of these two new quantities, the elasticity equations in the accelerated (primed) frame are

$$\rho \partial_t^2 y'_a + \nabla^b T'_{ab} = -\rho \frac{\vec{F}_a}{M} \cos(\omega t). \quad (\text{C6})$$

The right hand side is simply the inertial force associated with working in an accelerated frame.

The boundary conditions remain unchanged.

##### b. Step 2: Factor out all sinusoidal dependence

In the accelerated frame, we now assume all quantities oscillate sinusoidally in response to the sinusoidally-oscillating pressure profile and inertial force:

$$\begin{aligned} y'_a &= \bar{y}_a \cos(\omega t), \\ T'_{ab} &= \bar{T}_{ab} \cos(\omega t). \end{aligned}$$

Substituting these expressions into Eq. (C6), we find we can reconstruct a solution to the dynamic solution by solving the static partial differential equation

$$-\rho \omega^2 \bar{y}_a + \nabla^b \bar{T}_{ab} = -\rho \frac{\vec{F}_a}{M} \quad (\text{C7})$$

subject to force-free boundary conditions on all surfaces except the top surface, which is subjected to a *constant* pressure profile  $\bar{T}_{az}(\vec{r}, z = 0)$ .

##### c. Step 3: Approximate the problem as static in the accelerated frame

Finally, at sufficiently low frequencies (i.e. frequencies so low that sound crosses the cylinder many times within one period, as is the case for advanced LIGO; cf. notes 2 and 3), the first term in the accelerated-frame elasticity equations [i.e. the term  $\propto y'_a \omega^2$  in Eq. (C6)] can be neglected (cf., e.g., LT Sec. II). The remaining problem [i.e. Eq. (10)] can be interpreted precisely as equations for the static elastic response of a solid to an imposed pressure profile.

#### d. Summary

To summarize, then, we find an approximate solution for the elastic response of a solid to an imposed surface stress  $T_{az}$  at  $z = 0$  by

$$y_a = \cos(\omega t) \left[ -\rho \frac{\vec{F}_a}{M\omega^2} + \bar{y}_a \right] \quad (\text{C8a})$$

where  $\bar{y}_a$  is obtained as a solution to the static elastic equations in an accelerated frame

$$\nabla^b \bar{T}_{ab} = -\rho \frac{\vec{F}_a}{M} \quad (\text{C8b})$$

subject to the effective static surface stress  $\bar{T}_{az}$  and bulk acceleration  $\vec{F}_a/M$  given by

$$T_{az} = \bar{T}_{az} \cos(\omega t) \quad (\text{C8c})$$

$$\vec{F}_a \equiv - \int d^2r \bar{T}_{az}(\vec{r}, z=0) \quad (\text{C8d})$$

To summarize our conclusions on physical grounds, because the elastic response occurs much more rapidly than the surface pressure profile changes (i.e. because the sound crossing time is much shorter than the oscillation period of the imposed force), we can effectively treat the elastic response as instantaneous. The elastic solid moves slowly through a sequence of static configurations.

This quasistatic approximation, however, must be performed with care. If one neglects the dynamical terms entirely, as other authors working on this and related subjects have done<sup>37</sup>, then one finds elasticity equations without the bulk acceleration term. That equation is inconsistent with the static boundary conditions we impose.

## 2. Using the quasistatic elastic solution to simplify our thermoelastic noise integral

We can apply the quasistatic elastic solution we just developed [Eq. (C8)] to find the thermoelastic integral  $I_A$  [Eq. (9)] associated with our specific elastic model problem, where the surface stress imposed has (i)  $T_{az} = 0$  unless  $a = z$  and (ii)  $T_{zz} = -\cos(\omega t)F_oP(r)$  [Eq. (10c)]. Since the accelerated-frame transformation does

not change  $\Theta$  (i.e.  $\Theta = \Theta'$ ) and since  $\langle \cos^2(\omega t) \rangle = 1/2$ , we conclude that

$$I_A = \frac{2}{F_o^2} \int d^3r \langle |\nabla\Theta|^2 \rangle \approx \frac{1}{F_o^2} \int d^3r |\nabla\bar{\Theta}|^2, \quad (\text{C9})$$

where the approximation neglects terms which are small in the quasistatic limit (cf. notes 3 and 2).

## APPENDIX D: ON THE COMPLETENESS OF BASIS STATES FOR AN ARM CAVITY WITH TWO IDENTICAL, INFINITE MIRRORS

In this appendix, we demonstrate that the eigenproblem for two identical infinite mirrors [Eq. (13)] admits a complete set of orthogonal eigensolutions. In the text, we use the resulting eigensolutions as a basis for building perturbative expansions.

Simply, the eigenequation admits a complete set of orthonormal states because it is an eigenvalue problem for a *unitary* operator. Unitary operators always admit a complete set of orthogonal eigenvectors. The technical details for the infinite-dimensional ( $L^2$ ) proof we need here are far beyond the scope of this paper. However, the reader can understand the result by two simple arguments:

*Orthogonality of eigenvectors for unitary matrices I: Via hermitian intermediary:* From any unitary operator we can define a hermitian operator  $H = i \ln U$  (e.g., by a series expansion). The hermitian operator admits a complete set of orthogonal states. Hence so does  $U = \exp(-iH)$ .

*Orthogonality of eigenvectors for unitary matrices II: Directly:* Alternatively, a familiar argument can be applied to demonstrate that, if  $U$  is a unitary matrix, the eigenspaces associated with distinct eigenvalues are mutually orthogonal.

Let  $\lambda_a$  and  $|a\rangle$  denote all the eigenvalues and (normalized) eigenvectors of a unitary operator  $U$ . Since  $U^\dagger U = 1$ , we know the eigenvalues are pure phase:  $\langle a|U^\dagger U|a\rangle = |\lambda_a|^2 = 1$ . Further, Since  $U^{-1}$  has  $|a\rangle$  an eigenvector with eigenvalue  $1/\lambda_a = \lambda_a^*$ , we can show  $\langle b|U = \lambda_b \langle b|$  and thus

$$0 = (\lambda_a - \lambda_b) \langle b|a\rangle. \quad (\text{D1})$$

Therefore, eigenvectors associated with *distinct* eigenvalues are mutually orthogonal.

Furthermore, in each degenerate subspace, we can diagonalize to find an orthogonal basis. Therefore, for unitary matrices, all eigenvectors can be assumed orthonormal.

## APPENDIX E: SECOND-ORDER PERTURBATION THEORY FOR EIGENSTATES OF AN INDIVIDUAL ARM CAVITY

In this appendix, we develop second-order perturbation expansions which relate changes in shape of one spe-

<sup>37</sup> Because of the fluctuation-dissipation theorem, many other authors working on thermal and thermoelastic noise (e.g., Cerdonio and Conti [27]; Liu and Thorne [12]; ...) must solve a similar or identical elastic problem to deduce the effects of noise. And most choose to approach it using a similar quasistatic approximation, ignoring any dynamical effects. However, most make the quasistatic approximation before they go to the accelerated frame, rather than after. Only Liu and Thorne have correctly accounted for the effects of acceleration, though they add those effects in by hand later.



cific mirror of a symmetric cavity (the ETM) to changes in the resonant states in general (and to changes of the the ground state in particular) of that cavity.

Since the precise form of the eigenequation depends on how one chooses to represent the state (i.e. at what plane, in what direction), many alternative and equivalent perturbation expansions can be derived<sup>38</sup>. The form presented in this appendix is that developed by O’Shaughnessy; Sergey Strigin and Sergey Vyatchanin performed their calculations using an independently-derived (but provably equivalent) approach.

As in the text, in this section we make heavy use of standard quantum-mechanics operator notation for states and inner products, a notation described briefly in Section IC (cf., e.g., [8, 9, 10]).

### 1. Preliminaries: Setting up notation for the expansion

We study the effect of changes in height of mirror 2 on the solutions to the eigenequation (13) in the case of a *symmetric* cavity with *infinite* mirrors. For clarity and simplicity of notation, we redefine the eigenequation problem we perturb still further, into the following expression:

$$\eta |\psi\rangle = GTG |\psi\rangle . \quad (\text{E1a})$$

$$G \equiv e^{-ikL} G_1 G_+ , \quad (\text{E1b})$$

$$T \equiv e^{-i\delta_2} \equiv 1 + \delta T , \quad (\text{E1c})$$

$$\delta_2 \equiv 2k\delta h_2 . \quad (\text{E1d})$$

Here,  $\delta h_2$  is the change in the (inward-pointing) height of the far mirror (mirror 2) and  $\delta T \equiv T - 1$ . [The operator  $T$ , used only in this section, should not be confused with the truncation operators defined in Eq. (11).]

### 2. Perturbation theory expansion, expressed using operators

We construct a perturbation theory expansion by expanding both sides of the eigenequation Eq. (E1) in se-  
<sup>38</sup>The relationship between these expressions need not be transparent. For example, one can represent the eigenequation using states represented “halfway” through a reflection of one of the mirrors (a choice which conveniently renders the resulting equation always perfectly symmetric). The transformation between

ries, giving

$$(\eta_o + \varepsilon\eta_1 + \varepsilon^2\eta_2 + \dots) (\psi_o + \varepsilon\psi_1 + \dots) \quad (\text{E2})$$

$$= G(1 + \delta T)G (\psi_o + \varepsilon\psi_1 + \varepsilon^2\psi_2) ,$$

and then matching orders on both sides; in this expression,  $\varepsilon$  is a formal perturbation parameter, added to rescale the change in the reflection operator:  $\delta T(\varepsilon) = \varepsilon\delta T$ . When we work out order matching, we find (for  $P$  a projection orthogonal to the ground state  $\psi_o$ , also denoted  $|0\rangle$ ):

$$\eta = \eta_o + \langle 0 | \delta\tilde{T} | 0 \rangle \quad (\text{E3a})$$

$$+ \left\langle 0 \left| \delta\tilde{T} P \frac{1}{\eta_o - G^2} P \delta\tilde{T} \right| 0 \right\rangle ,$$

$$\psi = |0\rangle + \frac{1}{\eta_o - G^2} P \delta\tilde{T} |0\rangle \quad (\text{E3b})$$

$$+ \frac{1}{\eta_o - G^2} P \left[ \delta\tilde{T} - \langle 0 | \delta\tilde{T} | 0 \rangle \right] \frac{1}{\eta_o - G^2} P \delta\tilde{T} |0\rangle ,$$

where the operation  $\tilde{O}$  on an operator  $O$  is defined by

$$\tilde{O} \equiv GOG . \quad (\text{E4})$$

We can furthermore substitute into the above expression the expansion

$$\delta\tilde{T} \approx G \left( -i\delta_2 - \frac{1}{2}\delta_2^2 \right) G = -i\tilde{\delta}_2 - \frac{1}{2}G\delta_2^2G$$

to give us the final form of the second-order expansion of the state:

our representation and this one depends on the mirror height. Thus, when the mirror heights are perturbed, the relationship between these two representations involves a unitary transformation that depends on the perturbation.

$$\eta = \eta_o - i \langle 0 | \tilde{\delta}_2 | 0 \rangle - \frac{1}{2} \langle 0 | G\delta_2^2G | 0 \rangle - \left\langle 0 \left| \tilde{\delta}_2 P \frac{1}{\eta_o - G^2} P \tilde{\delta}_2 \right| 0 \right\rangle + O(\delta_2^3) .$$

$$\psi = |0\rangle - i \frac{1}{\eta_o - G^2} P \tilde{\delta}_2 |0\rangle - \frac{1}{2} \frac{1}{\eta_o - G^2} P G \delta_2^2 G |0\rangle - \frac{1}{\eta_o - G^2} P \left[ \tilde{\delta}_2 - \langle 0 | \tilde{\delta}_2 | 0 \rangle \right] \frac{1}{\eta_o - G^2} P \tilde{\delta}_2 |0\rangle + O(\delta_2^3) .$$

### 3. Perturbation theory expansion, expressed using basis states

As a practical matter, we compute the perturbation series expansion using not the operators themselves, but

rather through a finite collection of matrix elements of

the relevant operators relative to basis states. Therefore, we insert the identity operator, represented as a sum over all basis states (i.e.  $\mathbf{1} = \sum_k |k\rangle \langle k|$ ), at several points in the above expression. Since the basis states are eigenvectors of the propagation operator  $G$  and since the operator  $G$  is unitary, we know

$$G |k\rangle = \lambda_k |k\rangle, \quad (\text{E6a})$$

$$\langle k| G = \lambda_k \langle k|. \quad (\text{E6b})$$

---


$$|\psi\rangle = |0\rangle - i \sum_{k \neq 0} \frac{\lambda_o \lambda_k}{\eta_o - \eta_k} |k\rangle \langle k | \delta_2 | 0\rangle \quad (\text{E7b})$$

$$+ \sum_{k \neq 0} |k\rangle \frac{\lambda_o \lambda_k}{\eta_o - \eta_k} \left[ -\frac{1}{2} \langle k | \delta_2^2 | 0\rangle + \frac{\eta_o}{\eta_o - \eta_k} \langle k | \delta_2 | 0\rangle \langle 0 | \delta_2 | 0\rangle - \sum_{p \neq 0} \frac{\eta_p}{\eta_o - \eta_p} \langle k | \delta_2 | p\rangle \langle p | \delta_2 | 0\rangle \right] + O(\delta_2^3).$$

## APPENDIX F: PERTURBATION THEORY FOR CAVITIES BOUNDED BY TWO IDENTICAL SPHERICAL MIRRORS

For cavities bounded by spherical mirrors—that is, mirrors with height function  $h_{1,2} = r^2/2\mathcal{R}_{1,2}$ —the eigenfunctions are known and of simple, tractable Hermite-Gauss form. We can therefore perform perturbation-theory calculations analytically. In this appendix, we describe these basis states and their application to perturbation theory in greater detail.

### 1. Background: Notation and definitions

A spherical mirror of height  $h(r)$  is uniquely characterized by its radius of curvature  $\mathcal{R}$ :  $h = r^2/2\mathcal{R}$ . We consider two identical such mirrors, placed symmetrically at  $\pm L/2$ . We drive this cavity so it has  $kL/2\pi \gg 1$  wavelengths between the mirrors (so  $kL$  is to an excellent approximation independent of mirror shape).

#### a. Coordinate representation of eigenfunctions

The eigenfunctions for a cavity bounded by two identical spherical mirrors are known [15, 16, 17, 18, 19]:

$$\begin{aligned} \psi_{m,n} &= \sqrt{\frac{1}{2^{m+n} m! n!}} H_m \left( \frac{x}{A(z)} \right) H_n \left( \frac{y}{A(z)} \right) \\ &\times \frac{1}{\sqrt{\pi} A(z)} \exp \left[ -\frac{r^2}{2A(z)^2} \left( 1 - i \frac{z}{\bar{z}} \right) \right] \\ &\times \exp \left[ -i(N+1) \tan^{-1} \frac{z}{\bar{z}} + ikz \right]. \quad (\text{F1}) \end{aligned}$$

Therefore, we conclude that the eigenvalue changes as

$$\begin{aligned} \eta &= \eta_o \left( 1 - i \langle 0 | \delta_2 | 0\rangle \right) \quad (\text{E7a}) \\ &- \frac{1}{2} \langle 0 | \delta_2^2 | 0\rangle - \sum_{k \neq 0} \frac{\eta_k |\langle 0 | \delta_2 | k\rangle|^2}{\eta_o - \eta_k} + O(\delta_2^3) \end{aligned}$$

while the state changes according to the expansion

---

Here  $H_m$  are Hermite polynomials,  $A_o \equiv \sqrt{\bar{z}/k}$ ,  $N \equiv m+n$ ,  $g \equiv 1 - L/\mathcal{R}$ ,  $\theta = \cos^{-1} g$ ,  $k = (q\pi + \theta)/L$  for  $q$  a large integer, and

$$A(z)^2 \equiv A_o^2 \left( 1 + (z/\bar{z})^2 \right), \quad (\text{F2a})$$

$$\bar{z} \equiv \frac{L}{2} \sqrt{\frac{1+g}{1-g}}. \quad (\text{F2b})$$

In particular, at the mirror faces at  $z_{\pm} = \pm L/2$ , we have

$$z_{\pm}/\bar{z} = \pm \sqrt{\frac{1-g}{1+g}}, \quad (\text{F3a})$$

$$\tan^{-1}(z_{\pm}/\bar{z}) = \pm \frac{1}{2} \cos^{-1} g = \pm \theta/2, \quad (\text{F3b})$$

$$A(z_{\pm}) = \sqrt{\frac{L}{k}} \frac{1}{(1-g^2)^{1/4}}. \quad (\text{F3c})$$

#### b. Basis as eigensolutions of cavity

After some algebra, one can verify these states  $\psi_{m,n}$  are solutions to the round-trip eigenequation Eq. (13) [or equivalently Eq. (28)] with  $h_1(r) = h_2(r) = r^2/2\mathcal{R}$ , and

$$\lambda_{mn} = \sqrt{\eta_{mn}} = e^{-i\theta(m+n+1)}. \quad (\text{F4})$$

#### c. Establishing a quantum-mechanical correspondence

For technical reasons not discussed further here, the eigenfunctions of a cavity bounded by spherical mirrors correspond directly to the states of a 2-dimensional quantum-mechanical scalar nonrelativistic particle in a quadratic potential (i.e. a 2-d quantum simple harmonic

oscillator, or SHO). Like the SHO, the states are highly degenerate. If we index the states using their cartesian symmetry properties [i.e. express them as a Hermite-Gauss basis, as in Eq. (F1)], these quantum states of a SHO have the form  $|m, n\rangle = \Psi_m(x)\Psi_n(y)$  for

$$\Psi_n(x) \equiv \frac{1}{[\sqrt{\pi}A]^{1/2}} \frac{1}{\sqrt{2^n n!}} H_n\left(\frac{x}{A}\right) e^{-x^2/2A^2} \quad (\text{F5})$$

for  $A$  some length scale. Therefore, if we evaluate the fields at the mirror surface  $z = -L/2$  and define  $A = A(-L/2)$ , we find

$$\psi_{m,n}(x, y, z = -L/2) = e^{i\Phi_N} \Psi_m(x)\Psi_n(y) \quad (\text{F6a})$$

where  $\Phi_N$  is given by

$$\Phi_N = (N + 1)\theta/2 + (\text{independent of } N). \quad (\text{F6b})$$

Since the terms in  $\Phi_N$  which vary with  $N$  do not vary with position, we can establish a *correspondance* between matrix elements of SHO states and optical states for those operators which do not involve derivatives. Explicitly, if  $\mathcal{O}$  is an operator (e.g., some function of  $x$ ), then

$$\langle m, n | \mathcal{O} | \bar{m}, \bar{n} \rangle_{\text{opt}} = e^{i(\bar{N}-N)\theta/2} \langle m, n | \mathcal{O} | \bar{m}, \bar{n} \rangle_{\text{sho}}. \quad (\text{F7})$$

#### d. Creation and annihilation operators for SHO states

In quantum mechanics, many computations involving simple harmonic oscillator states can be rewritten in a more readable form by the use of creation and annihilation operators [8, 9, 10]. These simplifications occur because we can relate any excited state  $|0\rangle$  to the ground state via the action of these operators:

$$|m\rangle_{\text{sho}} = \frac{(a_x^\dagger)^m}{\sqrt{m!}} |0\rangle_{\text{sho}} \quad (\text{F8})$$

$$a_x^\dagger \equiv \frac{1}{\sqrt{2}} \left( \frac{x}{A} - A \frac{d}{dx} \right) \quad (\text{F9})$$

## 2. Tabulating useful matrix elements

When performing perturbation-theory calculations, we need the matrix elements of various operators (i.e.  $x$  and  $x^2$ ) relative to the Hermite-Gauss basis. These elements can be expressed as follows:

$$\begin{aligned} \langle m, n | x | \bar{m}, \bar{n} \rangle_{\text{opt}} & \quad (\text{F10a}) \\ &= e^{i(\bar{N}-N)\theta/2} \left\langle m, n \left| \frac{A(a_x + a_x^\dagger)}{\sqrt{2}} \right| \bar{m}, \bar{n} \right\rangle_{\text{sho}} \\ &= \frac{A}{\sqrt{2}} \delta_{n\bar{n}} \left[ e^{i\theta/2} \sqrt{\bar{m}} \delta_{m, \bar{m}-1} + e^{-i\theta/2} \sqrt{\bar{m}} \delta_{\bar{m}, m-1} \right] \end{aligned}$$

$$\begin{aligned} \langle m, n | x^2 | \bar{m}, \bar{n} \rangle_{\text{opt}} & \quad (\text{F10b}) \\ &= e^{i(\bar{N}-N)\theta/2} \left\langle m, n \left| \frac{A^2 (a_x + a_x^\dagger)^2}{2} \right| \bar{m}, \bar{n} \right\rangle_{\text{sho}} \\ &= \frac{A^2}{2} \delta_{n\bar{n}} \left[ e^{i\theta} \sqrt{m(m+1)} \delta_{m, \bar{m}-2} \right. \\ & \quad \left. + (2m+1) \delta_{m, \bar{m}} \right. \\ & \quad \left. + e^{-i\theta} \sqrt{\bar{m}(\bar{m}+1)} \delta_{\bar{m}, m-2} \right] \end{aligned}$$

In the above, we use the subscript *opt* to denote an optical state and *sho* to denote a SHO state.

## 3. Effects of tilt on beam state

If we tilt mirror 2 about the  $y$  axis, the mirror's height changes according to  $\delta_2 = 2kx\phi$  [cf. Eqs. (61) and (30)]. Using that expression in the two perturbative expansion expressions, Eqs. (32b) and (32c), and taking account of the above tools, we can find explicit expressions for the first and second order changes in the beam state evaluated at mirror 1.

$$|\psi^{(1)}\rangle = -|1, 0\rangle (\phi\sqrt{Lk}) \frac{e^{-i\theta/2}}{\sqrt{2}} \frac{1}{(1-g^2)^{3/4}} \quad (\text{F11})$$

$$|\psi^{(2)}\rangle = -|2, 0\rangle (\phi\sqrt{kL})^2 \frac{e^{i\theta}}{(1-g)\sqrt{2(1-g^2)}} \quad (\text{F12})$$

In performing the above calculation, we have explicitly substituted in  $A = A(z_\pm)$  from Eq. (F3c) and  $e^{i\theta} = g + i\sqrt{1-g^2}$  [derived from Eq. (F3b)] when appropriate.

## 4. Effect of displacement on beam state

When the mirror is displaced through a distance  $d$  in the  $x$  direction, the mirror height is perturbed from  $h(r) = r^2/2\mathcal{R}$  into

$$h'(r) = h(\vec{r} + s\hat{x}) = h(r) + \frac{xs}{\mathcal{R}} + \frac{s^2}{2\mathcal{R}}. \quad (\text{F13})$$

We can in a straightforward manner insert  $\delta h_{\text{disp}} = h' - h$  into the perturbative expansion for the state [Eq. (E7b)]; note that  $\delta h$  has terms both first and second order in  $\psi$ ; and thereby deduce the appropriate first and second order changes in the optical state of the cavity.

We will not provide a comprehensive calculation here. Instead, we note that the first-order changes in height  $\delta h$  due to tilt and displacement are identical, involving merely a change in factor:

$$\phi\sqrt{Lk} \rightarrow (s/b)(1-g). \quad (\text{F14})$$

Therefore, we deduce the first-order effect of a displacement of mirror 2 is

$$|\psi^{(1)}\rangle = -|1, 0\rangle (d/b) \frac{e^{-i\theta/2}}{\sqrt{2}} \frac{(1-g)}{(1-g^2)^{3/4}} \quad (\text{F15})$$

**APPENDIX G: POSTPROCESSING  
PERFORMED ON FINITE-ELEMENT  
COMPUTATIONS USED IN THERMOELASTIC  
NOISE INTEGRALS**

We used a commercial finite-element code, FEMLAB [22], to solve the fluctuation-dissipation-motivated axisymmetric elastic model problem presented in Eq. (10). This code expresses its solution for  $y^a$  in terms of a piecewise linear function. Unfortunately, the thermoelastic noise integral depends on second derivatives of  $y_a$ . Therefore, even though the FEMLAB program includes many useful tools to evaluate physically interesting quantities, we had to evaluate the thermoelastic noise integral ourselves. We therefore sent the FEMLAB output for  $y^a$  to a two-dimensional MATLAB array, then used our own MATLAB routines to generate expressions for  $|\nabla\Theta|^2$  and thus  $I_A$ .

The two groups performing this computation (Caltech and Moscow) each developed relatively independent postprocessing codes. In this appendix, we describe the Caltech postprocessing code.

### 1. Caltech postprocessing code

The Caltech group cobbled together a rough set of MATLAB routines to convert the finite-element representation of the response  $y^a$  to useful values for  $I_A$ . While this code contains more than a few kludges used to get it to work, we found the combination of the finite-element solution and this postprocessing routine gave answers for  $I_A$  that agreed well with and converged to the values of  $I_A$  for known, analytic solutions (i.e. the LT cylindrical solutions).

#### a. Postprocessing technique

1. *Preliminaries:* We used the FEMLAB finite-element code, with some number  $N$  elements, to find the elastic response of a frustum of front radius  $R_1$ , back radius  $R_2$ , and thickness  $H$ . We increased  $N$  until we felt comfortable with the resulting response curve. The FEMLAB code worked in cylindrical coordinates (i.e.  $r, z, \phi$ ), and assumed axisymmetry.
2. *Output to rectangular grid:* The code allowed us to extract the values of the displacement vector (components  $U = y_r$  and  $V = y_z$ ) at any point. We used this ability to obtain values of  $U$  and  $V$  on a rectangular grid. The code naturally provided smoothly extrapolated values of  $U$  and  $V$  when we asked for a point outside the volume simulated.

The total number of points on the rectangular grid was chosen to be comparable to  $N$ . Specifically, the

numbers of points in the  $r$  and  $z$  directions were chosen as  $\sqrt{NR_1/H}$  and  $\sqrt{NH/R_1}$ , respectively.

3. *Select cutoff region for grid:* Because we used a grid containing too large a region, we must provide a cutoff filter to select only those gridpoints which contain physical values. Furthermore, as a practical matter, the FEMLAB code gave odd results<sup>39</sup> when we evaluated the response at the edges of the computational domain. We therefore chose a cutoff filter which eliminated all exterior and “near-to-the-boundary” points.

This filter was applied repeatedly (i.e. during each derivative process). Because the filter was such a universal ingredient to each subsequent action, we will not mention each occurrence on which it is used in the following postprocessing.

4. *Compute expansion:* Using the relationship between  $\Theta$  and  $y^a$ , namely

$$\Theta = \partial_z V + \partial_r U + U/r \quad (\text{G1})$$

we compute  $\Theta$ . Derivatives are formed as centered differences, which are then interpolated (or, for the endpoints, extrapolated) back to the gridpoints. The values of  $U/r$  at  $r = 0$  are found by extrapolating the values of  $U/r$  for  $r \neq 0$ .

[To circumvent problems that arose due to dividing by small numbers near  $r = 0$ , we typically erased the values for  $\Theta$  we obtained on four gridlines near  $r = 0$  and replaced them by extrapolated values of the region immediately outside.]

5. *Compute  $|\nabla\Theta|^2$ :* Next, we computed the two derivatives  $\partial_r U$  and  $\partial_z V$  and used them to form

$$|\nabla\Theta|^2 = (\partial_r U)^2 + (\partial_z V)^2. \quad (\text{G2})$$

As before, derivatives were evaluated with centered differences which were interpolated to gridpoints.

6. *Compute  $I_A$ :* Finally, we used our own two-dimensional (Simpson’s rule) integrator to evaluate the two-dimensional integral

$$I_A = \int r dr dz |\nabla\Theta|^2, \quad (\text{G3})$$

which provides an explicit form for Eq. (9).

---

<sup>39</sup> In other words, we found NaN (i.e. “not a number”) answers from our code.

b. *Testing the result*

Our postprocessing code is far from polished. To insure the cutoff filter is operating properly and to otherwise guarantee that the results of the postprocessing code seem physically plausible, we usually plotted  $|\nabla\Theta|^2$  to verify that the integrand is indeed a well-behaved (i.e. smooth-looking) function.

Because we had a serious limitation on the number of points we could practically employ in a reasonable amount of desktop computing time ( $\sim \text{few} \times 10^4$ ), we did not perform systematic convergence testing. However, what testing we did, corroborated by comparisons between our numerical method and exact analytic solutions, suggests our results are relatively accurate. More critically, our computations agreed well with independent computations performed by Sergey Strigin and Sergey Vyatchanin.

## APPENDIX H: THERMOELASTIC NOISE OF HALF-INFINITE MIRRORS

To evaluate the thermoelastic noise associated with a given beam shape  $P(r)$ , we must evaluate the integral  $I_A$  [Eq. (9)] given the solution  $y^a$  to a model elasticity problem [Eq. (10)]. As discussed in Sec. V A 3, if the mirror is sufficiently large compared to the beam shape  $P(r)$ , we can effectively treat the mirror as half-infinite (i.e. filling the whole volume  $z < 0$ ) in the elasticity problem. In this case, the bulk acceleration term in the elasticity problem drops out [i.e.  $V_A \rightarrow \infty$  in Eq. (10a)] and we seek only the elastic response of a half-infinite medium to an imposed surface stress. This last problem has been discussed extensively in the literature — cf., e.g., [23, 24] — and there exist simple fourier-based computational techniques to generate and manage solutions. We apply these known solutions from the literature to evaluate the thermoelastic integral  $I_A$ .

### 1. Elastic solutions for the expansion ( $\Theta$ )

In the case of half-infinite mirrors, the response  $y^a$  to the imposed pressure profile  $P(r)$  can be found in the literature [cf. Eqs. (8.18) and (8.19) of Landau and Lifshitz's book on elasticity [23], where, however, the half-infinite volume is chosen *above* the  $z = 0$  plane rather than below; see also Nakagawa et al. [24], especially their Appendix A]. These expressions allow us to explicitly relate the expansion  $\Theta$  to the imposed pressure profile  $P(r)$ :

$$\Theta(\vec{r}, z) = \int G^{(\Theta)}(\vec{r}, z; r') P(r') d^2 r' \quad (\text{H1a})$$

$$G^{(\Theta)}(\vec{r}, z; \vec{r}_o) = -\frac{(1+\sigma)(1-2\sigma)zH(-z)}{2\pi E |(\vec{r}-\vec{r}_o)^2 + z^2|^{3/2}} \quad (\text{H1b})$$

where  $H(x)$  is a step function which is 1 when  $x > 0$  and 0 otherwise.

Because we have complete transverse translation symmetry, we can make our results more tractable by fourier-transforming in the transverse dimensions:

$$\tilde{\Theta}(K, z) \equiv \int e^{-i\vec{K}\cdot\vec{R}} \Theta(R, z) d^2 R, \quad (\text{H2})$$

$$\tilde{P}(\vec{K}) \equiv \int e^{-i\vec{K}\cdot\vec{R}} P(R) d^2 R. \quad (\text{H3})$$

For example, the convolution relating light intensity profile to the associated elastic response, Eq. (H1a), can be re-expressed as

$$\tilde{\Theta}(K, z) = G^\Theta(z, \vec{K}) \tilde{P}(\vec{K}) \quad (\text{H4})$$

$$\tilde{G}^{(\Theta)}(z, \vec{K}) = -\frac{(1+\sigma)(1-2\sigma)}{2\pi E} e^{-|Kz|}. \quad (\text{H5})$$

### 2. Thermoelastic integral $I_A$

Inserting the solution discussed above into Eq. (9) and using fourier-transform techniques to simplify the resulting integral, we find

$$I_A = \left( \frac{(1+\sigma)(1-2\sigma)}{2\pi E} \right)^2 \int d^2 \vec{K} |K| |\tilde{P}(K)|^2. \quad (\text{H6})$$

## APPENDIX I: CONFIGURATIONS WITH NONIDENTICAL FRUSTUM MIRRORS AND MESA-LIKE BEAMS

Physically the ETM and ITM need not be identical: while the ITM back face size is constrained to be above a certain radius (for a given mesa-beam  $D$ ) by diffraction losses, the ETM back face has no size restriction. Therefore, if we allow different mirrors, we introduce more parameters and therefore more possibilities for finding a mirror and beam configuration with very low noise.

Unfortunately, strictly speaking the mesa beams presented in this paper are designed specifically for identical cavities. Therefore, in the main text, when we explored how thermoelastic noise varied with mirror dimensions and shape, we restricted attention to cavities bounded by *identical* mirrors.

Nonetheless, we expect that *generic* flat-topped beams will always closely resemble the mesa-beam profile, with roughly the mesa-beam diffraction losses. Therefore, this appendix generalizes the computations of Sec. VI to include distinct ETM and ITM mirrors.

More specifically, we (i) assume that, for any  $D_1$  and  $D_2$ , there is some flat-topped beam whose intensity very closely mimics the mesa-beam intensity profile  $|u_{\text{mesa}}(r, D_1)|^2$  at mirror 1 and  $|u_{\text{mesa}}(r, D_2)|^2$  at mirror 2; (ii) select  $D_1$ ,  $D_2$ ,  $R_1$ , and  $R_2$  so the clipping approximation to the diffraction losses is 10 ppm at each mirror

face (Sec. IID); and (iii) use the resulting beam intensity profiles to compute the thermoelastic noise integrals  $I_1$  and  $I_2$  (Sec. VA). The power spectrum of thermoelastic noise for an interferometer with two identical arm cavities, each of which has an ITM like mirror 1 and an ETM mirror 2 can be expressed relative to the baseline [cf. Eq. (7)] by

$$S_h/S_h^{\text{BL}} = \frac{I_{\text{ITM}} + I_{\text{ETM}}}{2I_{\text{BL}}}. \quad (\text{I1})$$

### 1. Thermoelastic noise integral for ETM designs

The ETM mirror has only two design constraints: (i) its mass must be 40 kg and (ii) the diffraction losses off its front face must be less than or equal to 10 ppm. Table VI shows the value of the thermoelastic noise integral for various values of  $R_{p1}$ ,  $R_{p2}$ , and  $D$ , chosen to satisfy the various constraints (mirror mass 40 kg; diffraction losses off the front face of 10 ppm).

While we have complete freedom to adjust the back face size of the ETM, from the table, we see the back face size matters little so long as it is less than  $R_{p2} \lesssim 9$  cm. By fitting a quadratic to  $(D/b, I/I_{\text{BL}})$  [for only those ETM entries with  $R_{p2} \lesssim 9$ cm], we estimate the optimal ETM dimensions; our results are tabulated in Table VII.

In Table VII we also combine the optimal ETM with the optimal ITM and use Eq. (I1) to express the thermoelastic noise of a nonidentical-mirror configuration relative to the baseline. When the ETM can be different from the ITM, the optimal thermoelastic noise is significantly reduced (because the ETM inner radius can be larger).

### 2. Aside: Constructing mesa-like beams appropriate to nonidentical mirrors

In this appendix, we assume that for any  $D_1$  and  $D_2$ , there is some flat-topped beam whose intensity closely mimics the mesa-beam intensity profile  $|u_{\text{mesa}}(r, D_1)|^2$  at mirror 1 and  $|u_{\text{mesa}}(r, D_2)|^2$  at mirror 2. In fact, we may explicitly construct such a beam through a generalization of the mesa-beam proposal (though the authors have not numerically explored this possibility).

The mesa beams constructed in this paper were built by averaging minimal gaussian beams which all travelled *parallel* to the optic axis [cf. Eq. (5)]. More generally, we can construct mesa-like beams by averaging gaussians which travel at a position-dependent angle to the optic axis; for example, at mirror 1, we could choose the beams to have angle distribution

$$\phi(r) = \frac{R_2 - R_1}{L} \frac{r}{R_1}. \quad (\text{I2})$$

The resulting mesa-type beams will have power distributions at the two mirrors which closely resemble the

TABLE VI: The thermoelastic integral  $I$  for a frustum end test mass (ETM) and a Mexican-Hat Beam, in units of  $I_{\text{BL}} = 2.57 \times 10^{-28} \text{s}^4 \text{g}^{-2} \text{cm}^{-1}$ . The values of  $I/I_{\text{BL}}$  are estimated to be accurate to within one per cent.

$R_1$	$R_{p1}[\text{cm}]$	$R_{p2}[\text{cm}]$	$H[\text{cm}]$	$D/b$	$I/I_{\text{BL}}$	$\mathcal{L}_0[\text{ppm}]^a$
$R_{p1} - 8\text{mm}$	17.11	2.00	28.85	4.00	0.175	10
$R_{p1} - 8\text{mm}$	17.11	8.00	19.34	4.00	0.175	10
$R_{p1} - 8\text{mm}$	17.11	12.00	14.87	4.00	0.192	10
$R_{p1} - 8\text{mm}$	19.58	3.00	21.17	5.00	0.134	10
$R_{p1} - 8\text{mm}$	19.58	9.00	14.91	5.00	0.133	10
$R_{p1} - 8\text{mm}$	19.58	13.00	11.83	5.00	0.180	10
$R_{p1} - 8\text{mm}$	19.98	5.00	18.22	5.15	0.133	10
$R_{p1} - 8\text{mm}$	22.08	3.00	16.97	6.00	0.156	10
$R_{p1} - 8\text{mm}$	22.08	9.00	12.45	6.00	0.157	10
$R_{p1} - 8\text{mm}$	22.08	15.00	9.15	6.00	0.310	10
$R_{p1}$	13.94	5.00	32.93	3.00	0.333	10
$R_{p1}$	13.94	7.50	26.80	3.00	0.340	10
$R_{p1}$	13.94	10.00	21.96	3.00	0.345	10
$R_{p1}$	16.37	2.00	31.34	4.00	0.161	10
$R_{p1}$	16.37	4.00	27.33	4.00	0.160	10
$R_{p1}$	16.37	6.00	23.74	4.00	0.160	10
$R_{p1}$	16.37	8.00	20.63	4.00	0.160	10
$R_{p1}$	16.37	10.00	17.96	4.00	0.162	10
$R_{p1}$	16.37	12.00	15.70	4.00	0.173	10
$R_{p1}$	16.37	14.00	13.78	4.00	0.207	10
$R_{p1}$	18.85	1.00	25.45	5.00	0.112	10
$R_{p1}$	18.85	3.00	22.69	5.00	0.112	10
$R_{p1}$	18.85	5.00	20.12	5.00	0.112	10
$R_{p1}$	18.85	7.00	17.81	5.00	0.111	10
$R_{p1}$	18.85	9.00	15.56	5.00	0.113	10
$R_{p1}$	18.85	11.00	13.97	5.00	0.119	10
$R_{p1}$	18.85	13.00	12.41	5.00	0.144	10
$R_{p1}$	19.86	5.00	18.42	5.42	0.107	10
$R_{p1}$	21.36	3.00	18.04	6.00	0.116	10
$R_{p1}$	21.36	5.00	16.24	6.00	0.115	10
$R_{p1}$	21.36	7.00	15.39	6.00	0.115	10
$R_{p1}$	21.36	9.00	14.58	6.00	0.116	10
$R_{p1}$	21.36	12.00	11.15	6.00	0.133	10
$R_{p1}$	21.36	15.00	9.55	6.00	0.224	10

<sup>a</sup>Diffraction losses in each bounce off inner face of the test mass (radius  $R_1$ ), in ppm (parts per million).

power distributions of mesa beams: (i) they will be flat over a large central region, of size  $D_1$  at mirror 1 and size  $D_2 \approx D_1(R_2/R_1)$  at mirror 2; and (ii) they will fall off rapidly outside this region, with a falloff rate nearly the same as that of the minimal gaussian.

TABLE VII: Optimized test-mass and light beam configurations, their thermoelastic noise compared to the baseline. [A subset of this table appears as Table I in MBI [4], and as Table IV in this paper.]

Test Masses	Beam Shape	$\left(\frac{S_p}{S_h^{BL}}\right)_{TE}$
$\{R_{p1}, R_{p2}; H\}$		
BL: cylinders, $R = R_p - 8\text{mm}$ {15.7, 15.7; 13.0}	BL: Gaussian $r_o = 4.23\text{cm}$	1.000
BL: cylinders, $R = R_p - 8\text{mm}$ {15.7, 15.7; 13.0}	mesa $D/b = 3.73$	0.364
identical frustums, $R = R_p - 8\text{mm}$ {17.11, 12.88, 14.06}	mesa $D/b = 4.00$	0.207
different cones, $R = R_p - 8\text{mm}$ ITM{17.42, 13.18, 13.51}	MH $D/b = 4.00$	
ETM{19.96, $\lesssim 9.$ , $\gtrsim 14.$ }	$D/b = 5.15$	0.170
BL: cylinders, $R = R_p$ {15.7, 15.7; 13.0}	Gaussian $r_o = 4.49\text{cm}$	0.856
BL: cylinders, $R = R_p$ {15.7, 15.7; 13.0}	mesa $D/b = 3.73$	0.290
identical frustums, $R = R_p$ {17.29, 13.04, 13.75}	mesa $D/b = 4.39$	0.162
different cones, $R = R_p$ ITM{17.29, 13.04, 13.75}	MH $D/b = 4.39$	
ETM{19.91, $\lesssim 9.$ , $\gtrsim 14.$ }	$D/b = 5.42$	0.135

- [1] LIGO II Conceptual Project Book, available at <http://www.ligo.caltech.edu/docs/M/M990288-A1.pdf>
- [2] The LIGO Scientific Collaboration (LSC) maintains a website describing plans for the first-generation upgrade: <http://www.ligo.caltech.edu/advLIGO/>. This site was created for (and contains) the advanced LIGO NSF review. An older advanced LIGO website is at <http://www.ligo.caltech.edu/~ligo2/>.
- [3] Peter Fritschel maintained a website which provided a succinct summary of an older advanced LIGO design, including material parameters: <http://www.ligo.caltech.edu/~ligo2/scripts/12refdes.htm> (quoted 28-June-2003)
- [4] E. Ambrosio, R. O'Shaughnessy, S. Strigin, K. S. Thorne, and S. Vyatchanin, to be submitted to Phys. Rev. D, cited in text as MBI.
- [5] E. Ambrosio, R. O'Shaughnessy, S. Strigin, K. S. Thorne, and S. Vyatchanin, LIGO Report Number LIGO T030009, available at <http://ligo.caltech.edu>
- [6] E. D'Ambrosio, Phys. Rev. D **67**, 102004
- [7] R. Wald, *General Relativity*, University of Chicago Press, 1984.
- [8] P. A. M. Dirac, *The principles of quantum mechanics*, 4th edition (Oxford University Press, 1958)
- [9] L. D. Landau and E. M. Lifshitz, *Quantum Mechanics*, 3rd edition (Pergamon Press) 1977
- [10] J. S. Townsend, *A modern approach to quantum mechanics*, (McGraw-Hill, New York) 1992
- [11] V. Braginsky, M. Gorodetsky, and S. Vyatchanin, Phys. Lett. A **264**, 1 (1999).
- [12] Y. T. Liu and K. Thorne, Phys. Rev. D **62**, 1222002.
- [13] Y. Levin, Phys. rev. D **57**, 659 (1998)
- [14] R. D. Blandford and K. S. Thorne, *Applications of classical physics*, unpublished. Draft versions are available at <http://www.pma.caltech.edu/Courses/ph136/yr2002/index.html>
- [15] A. Siegman, *An Introduction to Lasers and Masers* (McGraw-Hill, 1971).
- [16] A. Siegman, *Lasers* (University Science, Mill Valley, 1986); errata URL: [http://www-ee.stanford.edu/~siegman/lasers\\_book\\_errata.txt](http://www-ee.stanford.edu/~siegman/lasers_book_errata.txt)
- [17] A. Yariv, *Quantum electronics*, 3rd edition (John Wiley & Sons, 1989).
- [18] L. Ronchi, *Optical resonators*, in *Laser physics handbook*, vol. 1, F. T. Arecchi and E. O. Schulz-Dubois, eds. (North-Holland Publishing, 1972)
- [19] F. M. Barnes, ed., *Laser Theory*, (IEEE Press, 1972)
- [20] R. G. Beausoleil and D. Sigg, J. Opt. Soc. Am. B **107**, 1597 (1997). Also available as LIGO Report Number P990004, available at <http://ligo.caltech.edu>
- [21] R. G. Beausoleil et al. LIGO Report Number P020026, available at <http://ligo.caltech.edu>
- [22] FEMLAB, described at <http://www.comsol.com>
- [23] L. Landau and E. M. Lifshitz, *Theory of elasticity*, 2nd edition (Pergamon Press, 1970)
- [24] N. Nakagawa et al., Phys Rev. D **65**, 102001.
- [25] K. Numata, CaJAGWR talk, pdf slides available at <http://cajagwr.caltech.edu/pdf/numata.pdf> and video available at <http://cajagwr.caltech.edu/scripts/numata.ram>
- [26] R. P. Feynman and A. H. Hibbs, *Quantum Mechanics and Path Integrals*, (McGraw-Hill, 1965).
- [27] M. Cerdonio et al, Phys Rev. D **63**, 082003 (2001).

